International Journal of Thermal Sciences 153 (2020) 106384

Contents lists available at ScienceDirect

International Journal of Thermal Sciences

journal homepage: http://www.elsevier.com/locate/ijts

Thermal performance of diffusion-bonded compact heat exchangers

A.P.C. Sarmiento [a,*], V.H.T. Soares [a], G.G. Carqueja [a], J.V.C. Batista [a], F.H. Milanese [a,b], M.B. H. Mantelli [a]

[a] Heat Pipe Laboratory, Department of Mechanical Engineering, Federal University of Santa Catarina, Florianópolis, SC, Brazil
[b] Department of Energy Engineering, Federal University of Santa Catarina, Araranguá, SC, Brazil

ARTICLE INFO

Keywords:
Compact heat exchanger
Diffusion bonding
Counter-flow heat exchanger

ABSTRACT

This work presents an experimental and theoretical evaluation of the thermal performance of a square straight diffusion-bonded stainless steel compact heat exchanger. A one-dimensional steady-state thermal model was proposed to predict the thermal characteristics of the heat exchanger. To validate the model and to study the thermal behavior of the heat exchanger, an experimental test apparatus was developed. The heat exchanger was tested in several combinations of Reynolds ranging from 2600 to 7500, representing transition to turbulent regimes. The temperatures were varied from 70 °C to 80 °C for the water and from 25 °C to 42 °C for the air, at the inlet of the heat exchanger, respectively. A good agreement between the experimental data and the analytical model was obtained.

1. Introduction

In the petroleum and process industries, shell and tube or variations represent about 35% of the total of the heat exchangers used, being by far the most popular technology [1,2]. Although these types of heat exchangers are reliable and robust, their large volumes and footprint area make them not appropriate to be used in some applications [1,3]. On the other hand, compact heat exchangers are highly efficient, as their main characteristic is their large heat transfer surface area for a fixed volume. Although these devices have evolved considerably lately to new efficient solutions, they still deserve a great deal of research around the world.

Compact heat exchangers have been developed for applications where requirements of small weight and space are mandatory, as encountered in aerospace, naval and automotive fields. In many heat exchangers especially the compact ones, hot and/or cold streams may flow through non-circular cross-section ducts, i.e., triangular or rectangular, among other geometries. The lengths of these ducts are usually small. The equipment may operate in several regimes, varying from laminar to turbulent.

Advanced heat exchangers, like the printed circuit (PCHE), are compact devices characterized by a large heat transfer surface to volume ratio, which presents high effectiveness and low terminal temperature difference. Generally, the compact heat exchanger is fabricated from a large number of plates with channels, chemically etched or water–jet machined [4,5]. After a stacking process, a diffusion bonding technique is applied for fabricating the cores. This technology allows for an excellent mechanical strength at the union interface, enabling these exchangers to support very large working pressures, which, in some situations may exceed 50 MPa [3,6]. Over the years, compact heat exchangers joined by diffusion bonding have been considered as an alternative to more conventional technologies for oil exploration platforms, advanced high-temperature reactors, concentrated solar power applications, synergetic air-breathing and rocket engine [7–10], among others. In this frame, a large volume of research effort has been dedicated to understand the thermohydraulics characteristics of diffusion-bonded compact heat exchangers, focusing on the channel geometry, channel topology, and fluid properties, employing both experimental and numerical approaches.

In recent years, compact heat exchangers with several channel topologies have been studied, namely: straight, zigzag, s-shape and airfoil shape. Mylavarapu et al. [11] evaluated the thermal-hydraulic performance of two straight semicircular printed circuit heat exchangers (PCHE) with helium as working fluid. A comparison of the model with the experimental data shows that the theoretical models underestimated the experimental Fanning friction factor. The Nusselt number calculated from their model is in good agreement with experimental Nusselt number, for Reynolds numbers up to 1700, when the onset of transition to turbulence is observed. For Reynolds number greater than 3000 a good agreement is observed for the Nusselt number model.

Seo et al. [12] studied the heat transfer and pressured drop

* Corresponding author.
E-mail addresses: andres@labtucal.ufsc.br (A.P.C. Sarmiento), marcia.mantelli@ufsc.br (M.B.H. Mantelli).

https://doi.org/10.1016/j.ijthermalsci.2020.106384
Received 11 April 2019; Received in revised form 21 February 2020; Accepted 16 March 2020
Available online 30 March 2020

Nomenclature

a	thickness of the intermediate plate m
$\sqrt{A}$	square root of the cross-section area m
$A_{channel}$	cross-section area of the channel m^2
A_f	total fin area m^2
A_{total}	total heat transfer area m^2
A_{wall}	average wall surface area m^2
b	channel height m
CoV	coefficient of variation
c_p	specific heat at constant pressure J/kg K
C_r	fluid capacity parameter
d_h	channel hydraulic diameter m
e	fin thickness m
F	volume field forces N/m^3
f	Darcy friction factor
H	height of the core m
H_{cell}	height of one cell m
H	heat transfer coefficient W/m^2 K
K_{td}	development correction factor
k	turbulence kinetic energy m^2/s^2
k_m	thermal conductivity of the material W/m K
k_f	fluid thermal conductivity W/m K
L	length of the core m
LMTD	logarithmic mean temperature difference K
ℓ	characteristic length m
$\dot{m}$	mass flow rate kg/s
m	fin efficiency parameter
n	number of channels per layer
N	number of layers for each side
M	total number of channels
Nu	Nusselt number
NTU	number of heat transfer units
P	wet perimeter of the channel m
Pr	Prandtl number
q	heat transfer rate W
Re	Reynolds number
R_{total}	overall thermal resistance K/W
$R_{convection}$	convection thermal resistance K/W
$R_{fouling}$	fouling thermal resistance K/W
T	temperature K
TC	thermal correction factor
t	t-Student parameter
UA	overall thermal conductance W/K
u	velocity m/s
V	total volume of the heat exchanger core m^3
V_{slice}	volume of one cell m^3
W	width of the core m
w	channel width m
x	cartesian components

Greek symbols

α	compactness parameter m^2/m^3
β	heat transfer surface area density m^2/m^3
β_d	ratio between the width and height of the rectangular channel
γ	interpolation parameter
Δ	denotes difference
ε	effectiveness of the heat exchanger
ε_f	fluctuation dissipation m^2/s^3
ζ	temperature difference tolerance
η_f	efficiency of the surface fin
η_o	overall efficiency of the surface fin
λ	total heat transfer surface density m^2/m^3
ν	degrees of freedom
ρ	fluid density kg/m^3
ψ	damping function
σ	porosity of the core

Subscript and abbreviations

cold	cold side
hot	hot side
exp	experimental
in	inlet
out	outlet
average	average value
wall	wall
min	minimum value
max	maximum value

characteristics of a straight semicircular microchannel PCHE, which was tested for Reynolds numbers up to 850, with water as the working fluid for both cold and hot sides.

Kwon et al. [13] experimentally studied the heat transfer coefficient in a straight semicircular mini-channel PCHE with a counterflow configuration. They tested the PCHE under various heat transfer conditions at cryogenic temperatures: single-phase, boiling and condensation. In the single-phase experiment, the tested Reynolds number was varied from 8500 to 17,000. They compared their data with Gnielinski [14] and Peng and Peterson [15] correlations. According to them, the Gnielinski correlation is able to predict the overall heat transfer coefficient within 10% while the Peng and Peterson [15] correlation compares with approximately 30% error on average.

Chu et al. [16] evaluated the thermohydraulic performance of PCHE with a straight semicircular channel with SCO_2 and water as heat exchanging fluids. Two experiments were developed; the first was a water and water combination to find the water correlations for the PCHE waterside. This test showed that the Gnielinski [14] correlation has a maximum and average errors of 13.2% and 8.6%, respectively for Reynolds number varying from 2800 to 6700. The second test used a combination of SCO_2 and water as fluids. The effects of thermal properties, pressure and the pseudo-critical effects on the thermal performance of the PCHE were analyzed in this test. For the SCO_2 side, correlations for calculating the Nusselt number as a function of fluid properties were proposed, valid for Reynolds number between 30,000 and 70,000.

Mortean et al. [5,7,17,18] developed a series of experimentally and numerical studies of a straight square diffusion bonded compact heat exchanger in a cross-flow configuration operating with water and air as heat exchanging fluids. They tested the compact heat exchanger in several combinations of Reynolds numbers up to 2496 and temperatures varying from 30 °C to 70 °C for the water and from 17 °C to 26 °C for the air, at the inlet of the heat exchanger.

Khalesi and Sarunac [19] developed a numerical analysis of the developing laminar flow and conjugate heat transfer in a rectangular microchannel with SCO_2 and liquid sodium as fluids. The values of friction coefficient and Nusselt numbers predicted by the numerical analysis were compared with analytical solutions from the literature. The numerical results show that a large variation in SCO_2 properties in the critical and pseudocritical regions affects the fluid flow and, consequently, the heat transfer. The effect of large properties variations is diminished for operating conditions away from the critical point.

Nikitin et al. [20] experimentally studied the heat transfer and pressure drop performance of a zigzag PCHE in an experimental SCO_2

loop. Pra et al. [21] showed that zigzag channels improve heat transfer with an increment on the friction factor. Chen et al. [22] evaluated the thermohydraulic performance of a semicircular zig-zag PCHE with helium as working fluid. Chen et al. [22] tested a PCHE with several inlet temperatures and pressure conditions varied up to 464 °C and 2.7 MPa for the cold side and 802 °C and 2.7 MPa for the hot side. The mass flow rate of the helium varied from 22 kg/h to 39 kg/h, representing Reynolds numbers from 1500 to 3558, covering the laminar and laminar to turbulent transition. According to them, if compared the heat transfer performance in straight semicircular channels, the zigzag channels provided a small advantage for the laminar flow regime however significant advantage near the transition regime. Chen et al. [23] studied the thermal-hydraulic performance of a zig-zag channel PCHE by means of numerical simulations. A comparison between the experimental data and numerical results showed good agreement for both heat transfer and pressure drop. From the analysis of the local temperature and velocity distributions, the fully developed condition was not reached due primarily to the topology of the zigzag channel. Moreover, the thermal boundary conditions showed that the temperature of the fluid and heat fluxes along the flow channel cross-section was not uniform. Nonetheless, the distribution of the bulk temperature of the helium along the flow direction was almost linear. In relation to the heat flux distributions, even if they were largely different at different segments, the tendency of the heat flux for each segment along flow direction was analogous. Meshram et al. [24] developed a comparative numerical simulation of semicircular straight and semicircular zigzag channels for the liquid flows in a fully turbulent regime. According to them, the hydraulic diameter plays important roles in the overall heat transfer and pressure drop for both channels. From the simulation results for the zigzag channel, it was found that a larger bend angle and smaller linear pitch perform better than a smaller bend angle and large linear pitch combination. Developed correlations derived from simulations were used in a one-dimensional thermal model of a PCHE. The results of a thermal model show that a volume of a PCHE with zigzag channels is significantly smaller than a straight PCHE.

Ngo et al. [25] investigated the thermal and hydrodynamical performance of an s-shaped fin PCHE by performing numerical analysis over a range of Reynolds numbers using computational fluid dynamics code with SCO_2 as the working fluid. They showed that the s-shaped channel provided up to seven times lower pressure drop while maintaining the heat transfer performance almost equal to that of a PCHE with zigzag channels. Kim et al. [26] numerically analyzed both the zigzag and airfoil-shape fin PCHE operating with SCO_2 as the working fluid. They concluded that the total heat transfer per unit volume of a PCHE does not depend on the channel shape and on the configuration. However, the pressure drop for the airfoil-shaped fin geometry was lower compared to the zigzag channel. Chen et al. [27] compared the comprehensive performance of PCHE with several NACA airfoil fin series and zigzag channels by means of computational fluid dynamics. According to them, the NACA airfoil has a reduction in pressure drop maintaining heat transfer performance. With a fixed vertical pitch, the heat transfer performance of NACA series airfoil fin PCHE increases as airfoil thickness increases. However, comprehensive performance, in which both flow and heat transfer are considered, degrades with increasing airfoil thickness. Among four NACA airfoils, NACA 0010 airfoil fin PCHE demonstrates the best overall performance. Wang et al. [28] studied experimentally the heat transfer of hybrid PCHE for concentrating solar power. The hybrid PCHE has airfoils fins on one side and straight rectangular channels on the other side. The heat transfer characteristics of the hybrid PCHE was experimentally investigated by using a ternary salt and a synthetic oil as the heat transfer fluids in the airfoil channel and the straight channel, respectively. The experimental data was obtained for the molten salt temperature ranging from 198 °C to 254 °C and Reynolds number range from 500 to 1548. Experimental Nusselt number was compared with other correlations for PCHE with straight and zigzag channels, showing that the airfoils fins have better heat transfer performance. Finally, two correlations for calculating the Nusselt number for PCHE with airfoils fins were developed.

Alvarez et al. [29] presented a complete pressure drop and second law analysis in two diffusion-bonded heat exchangers, the first with square straight channels, which is exactly the same considered in this work, and the second with square zig-zag channels. The total entropy generation numbers for the two channel geometries were compared and the optimum Reynolds operation number was determined for each geometry and for different experimental conditions.

As noted above, much of the work on compact heat exchanger joined by diffusion bonding is focused on computational and experimental evaluation operating under high temperatures and pressures (supercritical fluid), in laminar and fully turbulent Reynolds numbers. From a geometrical point of view, the majority of the works are focused on the evaluation of both continuous and discontinuous channels and their impact on the thermohydraulic behavior on compact heat exchangers. Most of the previous investigations studied the thermal characteristics of printed circuit heat exchangers with semicircular straight and non-straight channels. Note that, the effect of the mass flow distribution in the majority of these works was ignored. To the best of our knowledge, experimental performance evaluation of single-phase heat transfer on a square straight diffusion-bonded compact heat exchanger has been only analyzed for Reynolds number up to 2496 as shown by Mortean et al. [5,7,17,18].

Therefore, the main goal of this paper is to investigate the thermal characteristics of a straight square compact heat exchanger, where single-phase streams flow in the transition to turbulent regimes, in a diffusion bonded compact heat exchanger. To fulfill this goal, a mathematical method is proposed, where the results are compared with data obtained from experimental tests conducted in a diffusion-bonded heat exchanger constructed and tested for this purpose.

2. Compact heat exchanger theoretical model

In the current work, the heat transfer performance of a counter-flow compact heat exchanger joined by the diffusion bonding process is estimated theoretically. To fulfill this purpose, some correlations from the literature were validated with data from an experimental setup, constructed for testing a heat exchanger core, which was fabricated using the method developed by Mortean et al. [4,6]. The compact heat exchanger under analysis has a counter-flow configuration with square channels. Fig. 1 depicts a schematic of the investigated counter-flow heat exchanger, while Fig. 2 presents an illustration of the channel cross-section geometry, highlighting the parameters to be used in the models presented next.

According to Kays and London [30] and Hesselgreaves et al. [3], the subsequent parameters can be used to characterize the compact heat exchanger core, where, the most common is the hydraulic diameter, d_h, which, for the hot and cold side can be defined as, respectively:

$$d_{h,\mathrm{hot}} = \frac{4A_{\mathrm{channel,hot}}}{P_{\mathrm{hot}}} = \frac{2w_{\mathrm{hot}}b_{\mathrm{hot}}}{w_{\mathrm{hot}} + b_{\mathrm{hot}}} d_{h,\mathrm{cold}} = \frac{4A_{\mathrm{channel,cold}}}{P_{\mathrm{cold}}} = \frac{2w_{\mathrm{cold}}b_{\mathrm{cold}}}{w_{\mathrm{cold}} + b_{\mathrm{cold}}} \quad (1)$$

where w and b are the channel width and height and A_{channel} is the cross-section area of the channel, which is calculated as:

$$A_{\mathrm{channel,hot}} = w_{\mathrm{hot}}b_{\mathrm{hot}}A_{\mathrm{channel,cold}} = w_{\mathrm{cold}}b_{\mathrm{cold}} \quad (2)$$

The wet perimeter of the channel, P, can be estimated as:

$$P_{\mathrm{hot}} = 2(w_{\mathrm{hot}} + b_{\mathrm{hot}})P_{\mathrm{cold}} = 2(w_{\mathrm{cold}} + b_{\mathrm{cold}}) \quad (3)$$

The ratio between the total heat transfer area and the total volume is defined as the heat transfer surface area density of the core, $\beta = A/V$, being expressed as:

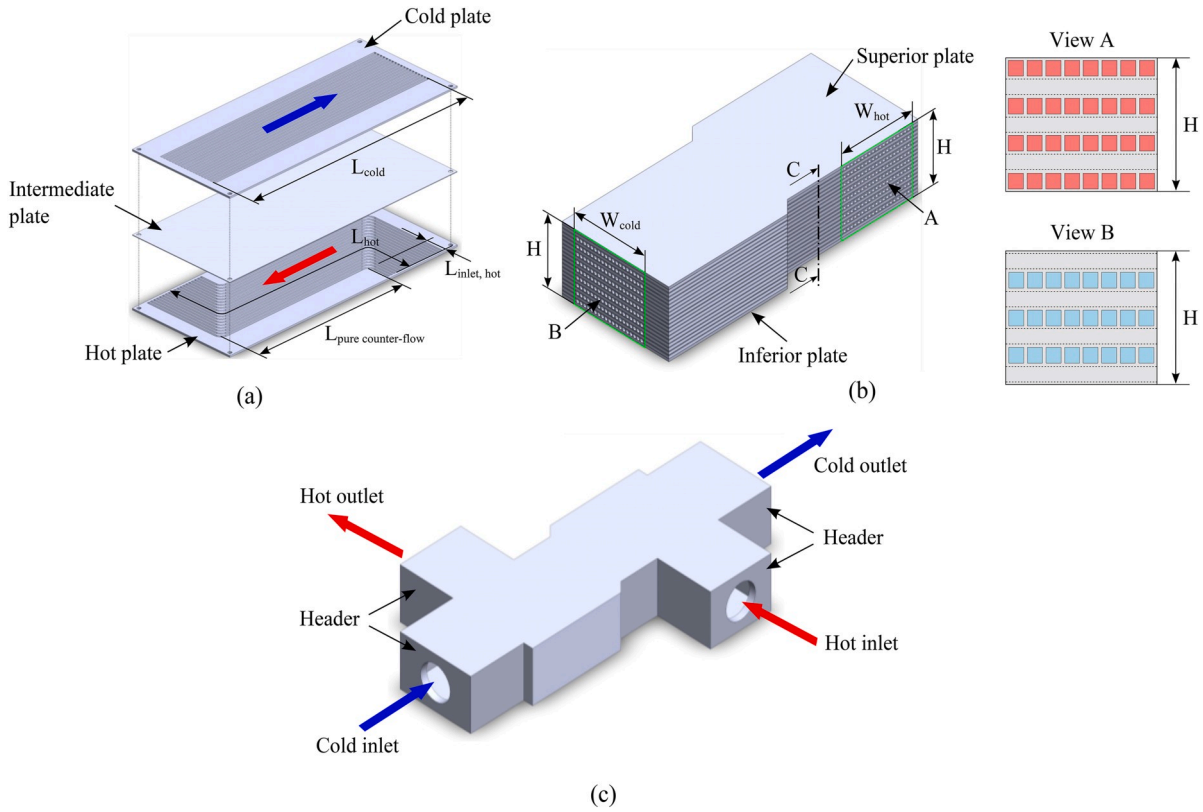

Fig. 1. Schematic illustration of the heat exchanger core with headers.

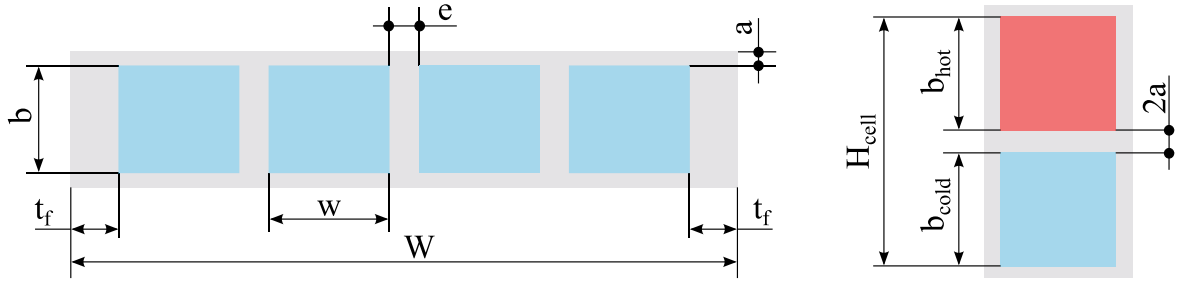

Fig. 2. Geometric parameters of the core.

$$\beta_{hot} = \frac{P_{hot}\ Ln_{hot}}{WLb_{hot}} = \frac{2(w_{hot} + b_{hot})n_{hot}}{b_{hot}W_{hot}} \beta_{cold} = \frac{P_{cold}\ Wn_{cold}}{WLb_{cold}} = \frac{2(w_{cold} + b_{cold})n_{cold}}{b_{cold}\ L_{cold}} \tag{4}$$

where L and W are the length and width of the core, respectively, while n is the number of channels per layer.

The compactness parameter, α, which is the ratio between the heat transfer area of one of the streams and the equipment volume, is defined as follows:

$$\alpha = \frac{P\ \ L\ \ n}{V_{slice}} = \frac{P\ \ L\ \ n}{W\ \ L\ \ H_{cell}} \rightarrow H_{cell} = b_{cold} + b_{hot} + a\alpha_{hot}$$
$$= \frac{b_{hot}\beta_{hot}}{b_{cold} + b_{hot} + a};\quad \alpha_{cold} = \frac{b_{cold}\beta_{cold}}{b_{cold} + b_{hot} + a} \tag{5}$$

where a is the thickness of the intermediate plate and H_{cell} is the height of one cell (cold and hot streams), as shown in Fig. 2. The total heat transfer area of each stream can be calculated as:

$$A_{total,hot} = \alpha_{hot}V;\quad A_{total,cold} = \alpha_{cold}VV = W\ H\ L \tag{6}$$

where V is the total volume of the heat exchanger core. The porosity of the core, σ, can be defined as the ratio between the free flow area and the total frontal area:

$$\sigma_{hot} = \alpha_{hot}\frac{d_{h,hot}}{4}\sigma_{cold} = \alpha_{cold}\frac{d_{h,cold}}{4} \tag{7}$$

The free flow area is calculated as:

$$A_{free,hot} = \sigma_{hot}(W_{hot}H)A_{free,cold} = \sigma_{cold}(W_{cold}H) \tag{8}$$

The total heat transfer surface density, λ, which is the main characteristic of the complete core and involves both sides, can be estimated as the total heat transfer area per total volume, is expressed by:

$$\lambda = \alpha_{hot} + \alpha_{cold} \tag{9}$$

2.1. Thermal model

The developed model in this work is similar to the one presented in [1,3,30]. To determine the overall thermal resistance of the heat exchanger, a thermal circuit model is applied, where the following hypotheses are assumed: 1) thermal radiation and natural convection are neglected; 2) fluid and solid properties are evaluated at their average

temperatures; 3) incompressible fluid flow; 4) steady-state heat transfer; 5) fluid flow in transition and turbulent regimes and 6) the fluid is uniformly distributed among the channels and has a uniform velocity profile at the inlet channels.

The overall thermal resistance can be expressed as a function of thermal resistances, where a schematic representation is shown in Fig. 3. According to Hesselgreaves et al. [3], the overall thermal resistance can be calculated as a sum of the convection, fouling and wall resistances.

The overall thermal conductance can be calculated as follows [1]:

$$\mathrm{UA} = R_{\mathrm{total}}^{-1} = \left(R_{\mathrm{convection,hot}} + R_{\mathrm{convection,cold}} + R_{\mathrm{wall}} + R_{\mathrm{fouling,hot}} + R_{\mathrm{fouling,cold}}\right)^{-1} \mathrm{UA} = R_{\mathrm{total}}^{-1} = \left(\frac{1}{\eta_{o,\mathrm{hot}} h_{\mathrm{hot}} A_{\mathrm{total,hot}}} + \frac{1}{\eta_{o,\mathrm{cold}} h_{\mathrm{cold}} A_{\mathrm{total,cold}}} + \frac{a}{k_{\mathrm{m}} A_{\mathrm{wall}}} + \frac{R_{d,\mathrm{hot}}^{''}}{\eta_{o,\mathrm{hot}} A_{\mathrm{total,hot}}} + \frac{R_{d,\mathrm{cold}}^{''}}{\eta_{o,\mathrm{cold}} A_{\mathrm{total,cold}}}\right)^{-1} \tag{10}$$

where $R_d^{''}$, η_o, A_{wall}, h, k_{m} are the fouling factor, overall efficiency of the surface, average wall surface area, heat transfer coefficient and thermal conductivity of the material, respectively. Rearranging Equation (10) and neglecting the fouling factor for both hot and cold sides, the overall thermal conductance is rewritten as:

$$\mathrm{UA} = \left(\frac{1}{\eta_{o,\mathrm{hot}} h_{\mathrm{hot}} A_{\mathrm{total,hot}}} + \frac{1}{\eta_{o,\mathrm{cold}} h_{\mathrm{cold}} A_{\mathrm{total,cold}}} + \frac{a}{k_{\mathrm{m}} A_{\mathrm{wall}}}\right)^{-1} \tag{11}$$

As shown in Fig. 4, the distribution of the hot and cold heat exchanger channels are periodical. Therefore, the heat exchanger is divided into repeating modules, which comprises a cell with half volume of a cold fluid channel from one plate, a partition plate and half of a hot fluid channel from the adjacent plate. The core of the heat exchanger can be modeled as a series of finned plates, where the fins are located between the hot or cold channels.

Temperature gradients along the fins reduce the overall efficiency, η_o. The overall efficiency of a set of fins can be estimated as a function of one fin efficiency, η_f, by the following expression [30]:

$$\eta_{o,\mathrm{hot}} = 1 - \frac{A_{\mathrm{f,hot}}}{A_{\mathrm{total,hot}}}\left(1 - \eta_{f,\mathrm{hot}}\right) \eta_{o,\mathrm{cold}} = 1 - \frac{A_{\mathrm{f,cold}}}{A_{\mathrm{total,cold}}}\left(1 - \eta_{f,\mathrm{cold}}\right) \tag{12}$$

where A_{f} is the total fin area. The ratio between total fin area, A_{f}, and the total heat transfer area, A_{total}, can be estimated as:

$$A_{\mathrm{f,hot}} = A_{\mathrm{total,hot}}\left(\frac{b_{\mathrm{hot}}}{b_{\mathrm{hot}} + w_{\mathrm{hot}}}\right) A_{\mathrm{f,cold}} = A_{\mathrm{total,cold}}\left(\frac{b_{\mathrm{cold}}}{b_{\mathrm{cold}} + w_{\mathrm{cold}}}\right) \tag{13}$$

Considering fins, with constant cross-section area and with negligible heat transfer in the tip, the efficiency of the fin can be given by [30]:

$$\eta_{f,\mathrm{hot}} = \frac{\tanh(m_{\mathrm{hot}} b_{\mathrm{hot}}/2)}{m_{\mathrm{hot}} b_{\mathrm{hot}}/2} \eta_{f,\mathrm{cold}} = \frac{\tanh(m_{\mathrm{cold}} b_{\mathrm{cold}}/2)}{m_{\mathrm{cold}} b_{\mathrm{cold}}/2} \tag{14}$$

where m is the fin efficiency parameter, expressed as:

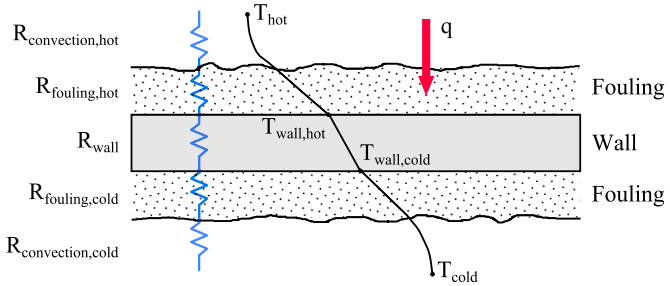

Fig. 3. Overall thermal resistance network.

$$m_{\mathrm{hot}} = \sqrt{\frac{2h_{\mathrm{hot}}}{k_{\mathrm{m}} e_{\mathrm{hot}}}} m_{\mathrm{cold}} = \sqrt{\frac{2h_{\mathrm{cold}}}{k_{\mathrm{m}} e_{\mathrm{cold}}}} \tag{15}$$

The terms h_{hot} and h_{cold} are the average heat transfer coefficients and they are related to the Nusselt number as, respectively:

$$h_{\mathrm{hot}} = \frac{k_{f,\mathrm{hot}} \mathrm{Nu}_{\sqrt{A},\mathrm{hot}}}{\sqrt{A}_{\mathrm{hot}}} h_{\mathrm{cold}} = \frac{k_{f,\mathrm{cold}} \mathrm{Nu}_{\sqrt{A},\mathrm{cold}}}{\sqrt{A}_{\mathrm{cold}}} \tag{16}$$

where $\mathrm{Nu}_{\sqrt{A}}$ is the Nusselt number, k_f is the fluid thermal conductivity and, $\sqrt{A}$ is the characteristic length. According to Hesselgreaves et al. [3] and Shah and London [31], a uniform heat flux (UHF) boundary condition can be used as a good approximation for representing the heat transfer in compact heat exchangers.

The number of heat transfer units, NTU, is defined as:

$$\mathrm{NTU} = \frac{\mathrm{UA}}{C_{\mathrm{min}}}; \quad C_{\mathrm{r}} = \frac{C_{\mathrm{min}}}{C_{\mathrm{max}}} = \frac{\left(\dot{m} c_p\right)_{\mathrm{min}}}{\left(\dot{m} c_p\right)_{\mathrm{max}}} \tag{17}$$

where C_{r} is the fluid capacity parameter, $\dot{m}$ is the mass flow rate and c_p is the specific heat at constant pressure. Considering no heat losses to the surroundings, the heat transfer rate, q, can be calculated as:

$$q = \dot{m}_{\mathrm{hot}} c_{p,\mathrm{hot}} \left(T_{\mathrm{hot,in}} - T_{\mathrm{hot,out}}\right) q = \dot{m}_{\mathrm{cold}} c_{p,\mathrm{cold}} \left(T_{\mathrm{cold,out}} - T_{\mathrm{cold,in}}\right) \tag{18}$$

where T is the fluid temperature. The heat exchanger effectiveness is expressed as the ratio between the heat transfer rate to the thermodynamically maximum heat transfer rate:

$$\varepsilon = \frac{q}{q_{\mathrm{max}}} = \frac{C_{\mathrm{hot}}\left(T_{\mathrm{hot,in}} - T_{\mathrm{hot,out}}\right)}{C_{\mathrm{min}}\left(T_{\mathrm{hot,in}} - T_{\mathrm{cold,in}}\right)} \varepsilon = \frac{q}{q_{max}} = \frac{C_{\mathrm{cold}}\left(T_{\mathrm{cold,out}} - T_{\mathrm{cold,in}}\right)}{C_{\mathrm{min}}\left(T_{\mathrm{hot,in}} - T_{\mathrm{cold,in}}\right)} \tag{19}$$

The effectiveness of the heat exchanger can be written as a function of the heat transfer units, NTU, the ratio between the smallest and the largest capacity rates, C_{r} and the flow arrangement [3,30]. For a heat exchanger with a counter-flow, the effectiveness, ε, can be respectively expressed as:

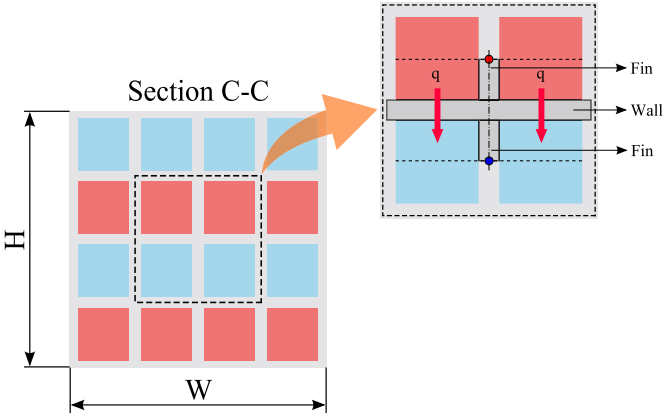

Fig. 4. Cross-sectional heat exchanger section with wall and fins.

$$\varepsilon = \begin{cases} \dfrac{1 - exp[-\mathrm{NTU}(1-C_r)]}{1 - C_r\, exp[-\mathrm{NTU}(1-C_r)]} \rightarrow C_r < 1 \\ \dfrac{\mathrm{NTU}}{1+\mathrm{NTU}} \rightarrow C_r = 1 \end{cases} \tag{20}$$

The outlet temperatures for both hot and cold streams were estimated through an energy balance, Equation (18), and they are expressed as:

$$T_{\mathrm{cold,out}} = T_{\mathrm{cold,in}} + \frac{q}{\dot{m}_{\mathrm{cold}} c_{p,\mathrm{cold}}} \quad T_{\mathrm{hot,out}} = T_{\mathrm{hot,in}} - \frac{q}{\dot{m}_{\mathrm{hot}} c_{p,\mathrm{hot}}} \tag{21}$$

As presented in Hesselgreaves et al. [3], for the calculation of the wall temperatures on a heat exchanger with uniform wall temperature the following equations can be used:

$$\begin{aligned} T_{\mathrm{wall,hot}} &= \frac{T_{\mathrm{hot,in}} + T_{\mathrm{hot,out}}}{2} - q\left(R_{\mathrm{convection,hot}} + R_{\mathrm{fouling,hot}}\right) T_{\mathrm{wall,cold}} \\ &= \frac{T_{\mathrm{cold,in}} + T_{\mathrm{cold,out}}}{2} + q\left(R_{\mathrm{convection,cold}} + R_{\mathrm{fouling,cold}}\right) \end{aligned} \tag{22}$$

In our case, as stated above, a uniform heat flux boundary condition is assumed. However, Equation (22) is still valid as the temperature gradient between the inlet and outlet side on the water stream, is very small. Besides, the wall temperature calculated with Equation (22) is used only to estimate the thermal correction factor, and very small influences on the Nusselt number are expected.

2.2. Nusselt number models

Equation (16) requires a model for calculating the Nusselt number. Several models from literature, valid for the transition region, can be selected and used.

Gnielinski [14,32] proposed the following correlation for calculating the Nusselt number in the transition and turbulent regimes, which is actually a modification of an equation proposed by Petukhov [33]:

$$\mathrm{Nu}_{d,T} = \mathrm{TC}\ \frac{K_{\mathrm{td}}(f/8)(\mathrm{Re}_d - 1000)\mathrm{Pr}}{1 + 12.7(f/8)^{1/2}\left(\mathrm{Pr}^{2/3} - 1\right)};\ \rightarrow 4000 < \mathrm{Re}_d < 1\times 10^6;\ \ 0.5 < \mathrm{Pr} < 2000 f = [1.82(\log_{10}\mathrm{Re}_d) - 1.64]^{-2} K_{\mathrm{td}} = 1 + \left(\frac{d}{L}\right)^{2/3};\ \ \mathrm{TC} = \begin{cases} \left(\dfrac{\mathrm{Pr}}{\mathrm{Pr}_{\mathrm{wall}}}\right)^2 & \text{if liquid} \\ 1 & \text{if the gas is cooled} \\ \left(\dfrac{T}{T_{\mathrm{wall}}}\right)^{0.45} & \text{if the gas is heated} \end{cases} \tag{23}$$

where TC is the thermal correction factor, as proposed by Hufschmidt and Burck [34], f is the Darcy friction factor model developed by Filonenko [35], K_{td} is development correction factor, which accounts for fully developed velocity profile, but undeveloped thermal profile at the entrance [36], Pr is the Prandtl number and Re_d is the Reynolds number based on the duct diameter. For the transition region, Gnielinski [14] proposed the use of a linear interpolation, with the following form:

$$\mathrm{Nu}_d = (1-\gamma)\mathrm{Nu}_{d,2300} + \gamma \mathrm{Nu}_{d,4000} \tag{24}$$

where

$$\gamma = \frac{\mathrm{Re}_d - 2300}{4000 - 2300};\ \ 0 \le \gamma \le 1 \tag{25}$$

The Nusselt number for $\mathrm{Re}_d = 2300$, is calculated using the well-known Gnielinski [32] correlations for the laminar flow, while, for $\mathrm{Re}_d = 4000$, it is determined by Equation (23).

Taler [37] developed a correlation for the transition and turbulent flow regimes in circular pipes, which has a similar form of Gnielinski correlation. The main difference is that Taler also considered the laminar flow regime, for both uniform heat flux (UHF) and uniform wall temperature (UWT) boundary conditions. Taler's [37] correlations is given by:

$$\mathrm{Nu}_{d,T} = \mathrm{Nu}_{d,l}(\mathrm{Re}_d = 2300) + \mathrm{TC}\frac{K_{\mathrm{td}}(f/8)(\mathrm{Re}_d - 2300)\mathrm{Pr}^{1.008}}{1.08 + 12.39(f/8)^{1/2}\left(\mathrm{Pr}^{2/3} - 1\right)};\ \ 2300 < \mathrm{Re}_d < 1\times 10^6;\ \ 0.1 < \mathrm{Pr} < 1000 \tag{26}$$

where $\mathrm{Nu}_{d,l}$ ($\mathrm{Re}_d = 2300$) is the Nusselt number for the laminar flow at $\mathrm{Re}_d = 2300$ for UHF or UWT boundary conditions and it depends if the flow is developed or under development. TC, K_{td}, and f are calculated using the expressions presented in Equation (23). Taler [37] reviews several correlations for calculating the Nusselt number in the laminar regime and recommends the use of the Gnielinski [32] correlation for the laminar flow.

Sarmiento et al. [38] proposed a correlation for estimating the Nusselt number in the transition region, based on the square root of the cross-sectional area, with the form:

$$\begin{aligned} \mathrm{Nu}_{\sqrt{A}} &= \left[\mathrm{Nu}_{\sqrt{A},L}^{m_c} + \left(\frac{\Psi}{\mathrm{Nu}_{\sqrt{A},L}^2} + \frac{1}{\mathrm{Nu}_{\sqrt{A},T}^2} \right)^{-\frac{m_c}{2}} \right]^{\frac{1}{m_c}} \Psi \\ &= \exp\left[-\frac{\left(\mathrm{Re}_{\sqrt{A},\mathrm{critical}} - \mathrm{Re}_{\sqrt{A}}\right)^2}{B^2} \right] \end{aligned} \tag{27}$$

where $\mathrm{Nu}_{\sqrt{A}}$ is the Nusselt number, $\mathrm{Nu}_{\sqrt{A},L}$ is the Nusselt number for low (laminar) Reynolds number, $\mathrm{Nu}_{\sqrt{A},T}$ is the Nusselt number for high (turbulent) Reynolds number. Ψ is a damping function, m_c is the asymptotic constant, $\mathrm{Re}_{\sqrt{A},\mathrm{critical}}$ is the critical Reynolds number, B is a constant. The Nusselt number for laminar flow is calculated by Muzychka and Yovanovich [39] model and for turbulent flow is calculated by the Gnielinski [14,32] model. For the case of uniform heat flux, m_c, B, and, $\mathrm{Re}_{\sqrt{A},\mathrm{critical}}$ are equal to 12, 425 and 1700, respectively.

2.3. Methodology to determine the heat exchanger conductance

Based on the equations described above one can estimate the thermal behavior of a diffusion-bonded compact heat exchanger by means of an iterative calculation. The flowchart used in this calculation is presented in Fig. 5. The input data are the inlet temperatures, pressures, and flow rates, for both fluids. Initially, the value for effectiveness is supposed to be 0.5. Using Equation (19), the outlet temperatures are estimated. Based on the outlet temperatures, the average temperature of the cell (see Fig. 4) can be calculated. With the average temperatures and inlet pressures, the fluid properties for both flows can be determined using the CoolProp library [40]. Reynolds number, dimensionless thermal and hydrodynamical lengths are calculated using these properties. Based on these data, the Nusselt number is estimated, using Equations (23), (26) and (27) and so, the convection heat transfer coefficients (Equation (16)) are determined. Equations (11) and (17) are employed to calculate the overall thermal conductance and the NTU parameter, respectively. This procedure is repeated until the temperature difference at the outlet, between the updated (iteration i+1) and the previous iteration (iteration i) satisfies the following relationship:

$$\zeta = \left| \frac{T_{\mathrm{out},i+1} - T_{\mathrm{out},i}}{T_{\mathrm{out},i}} \right| \times 100 < 10^{-8} \tag{28}$$

where ζ is the temperature difference tolerance.

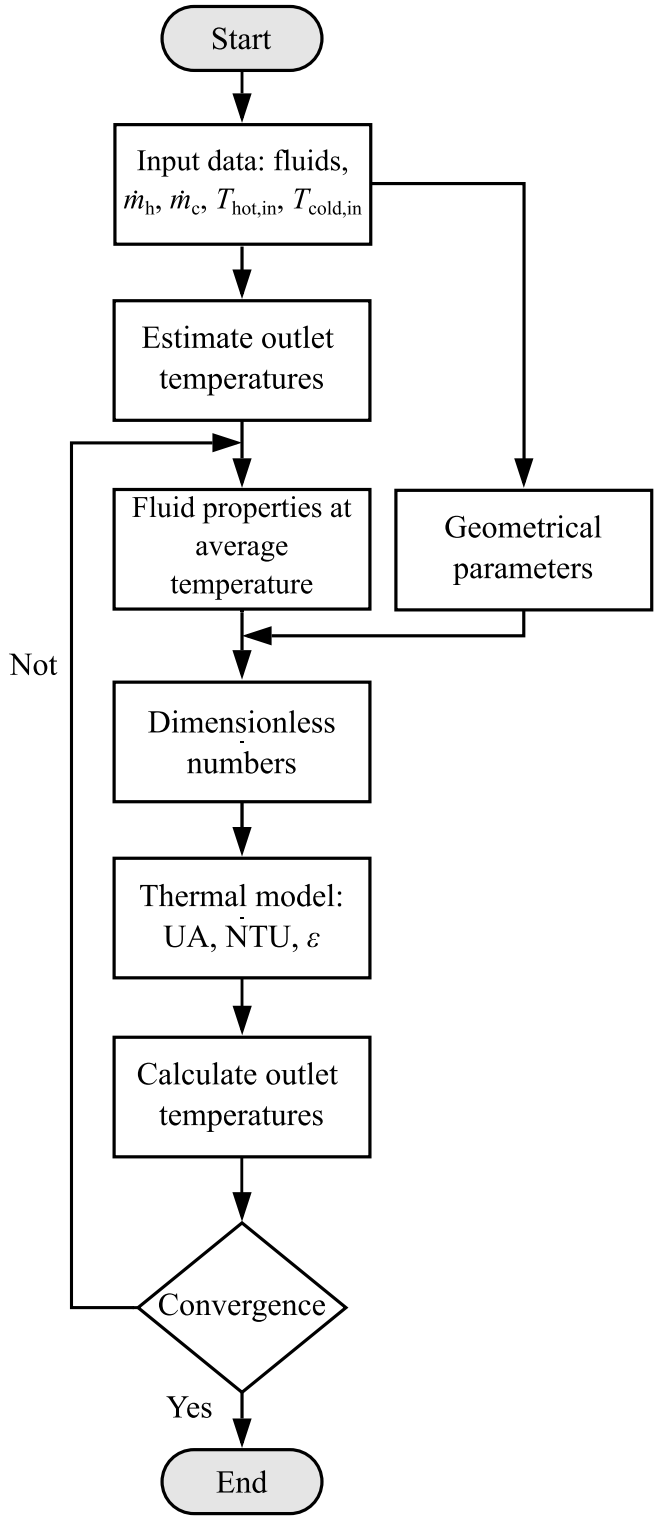

Fig. 5. Flowchart for calculating heat exchanger thermal parameters.

3. Experimental setup

3.1. Compact heat exchanger fabrication

A compact heat exchanger was fabricated using flat plates, which were water-jet machined in a comb shape. These plates are stacked alternately with intermediate not machined flat plates. The channels are formed by sandwiches between flat intermediate and comb-like machined plates. After the stacking process, the core was joined by diffusion bonding technique using an appropriate furnace, able to provide a high vacuum (10^{-6} Torr), high pressure (up to 2500 kN) and high temperature (up to 1400 °C). The yielding core is a monolithic heat exchanger block, with a strength similar to the base material. The heat exchanger was fabricated from 3 mm thick 316L stainless steel plates and 1 mm thick, 316L stainless steel for the intermediate not machined flat plates. The cross-sections of the channels of the heat exchanger are square, of 3 mm of edge. Each machined plate provides 19 channels and 9 plates are provided for the cold and 9 for the hot streams.

As shown in Fig. 1, the heat exchanger works in a counter-flow configuration. However, to allow for the installation of the headers, the channels of the hot side have a 90-degree bend for both entrance and exit regions, leaving a straight center section with a total flow length of 363 mm. The cold channels were straight with a total flow length of 344 mm. Other design parameters of the compact heat exchanger are shown in Table 1. After the heat exchanger core was fabricated, headers were welded to the core, to finish the construction of the compact heat exchanger prototype.

As shown in Table 1, the dimensions of the compact heat exchanger are in concordance with previous well succeed compact heat exchangers developed by Mortean et al. [5,7,17,18], which were fabricated by water-jet cutting technology.

3.2. Experimental test facility

Experimental tests were performed to examine the steady-state thermal performance of the described compact heat exchanger. Fig. 6 shows a 3D layout of the experimental facility. The experimental setup was composed of a hot and a cold branches and their components, a test section, and a control, acquisition, and processing systems. Both branches, hot and cold, worked with air and with water.

Fig. 7 illustrates both the cold and hot branches. Fig. 7a and b show the cold branch and the high-power fan. The cold branch was composed of a high-power centrifugal fan, stainless steel pipes, the cold flow tubing and a Coriolis flowmeter (ELITE CMF200 M) with an accuracy equal to 0.05% for the tested all the experimental test.

On the other hand, Fig. 7c shows the hot branch, which is composed of an expansion tower, a hydraulic pump, a reservoir, four electric heaters (maximum power of 60 kW), rubber hoses, stainless steel pipes, a hot flow tubing and, an electromagnetic flowmeter (Rousemout-8732) with an accuracy of ±0.50% for all the tested conditions. Finally, the set up provides a testing section, where the heat exchanger was installed and tested. The temperatures of the inlets and outlets of the hot and cold streams were monitored by four RTDs (Pt-100 P-M-1/3-1/8-6-1/8-T3 model) with an accuracy of 0.1 °C and 0.27 °C at 0 °C and 100 °C, respectively. The pressure was measured by two pressure transducers (OMEGATM PX409 series) with an accuracy of ±0.50% in full span.

Table 1
Design parameters of the compact heat exchanger.

Parameter	Hot side	Cold side
Channel pitch (mm), b	3	3
Channel width (mm), w	3	3
Intermediate plate thickness (mm), a	1	1
Fin thickness (mm), e	1.5	1.5
Hydraulic diameter (mm), d_h	3	3
Square root of the cross-sectional area, diameter (mm), $\sqrt{A}$	3	3
Number of layers, N	9	9
Number of channels in each plate, n	19	19
Channel cross-sectional area (mm^2), $A_{channel}$	9	9
Total flow length of the plate (mm), L	363	344
Entrance length (mm), L_{inlet}	23	0
Exit length (mm), L_{outlet}	23	0
Core width (mm), W	88	88
Core height (mm), H	72	72
Pure counter flow length (mm), $L_{counter\text{-}flow}$	210	

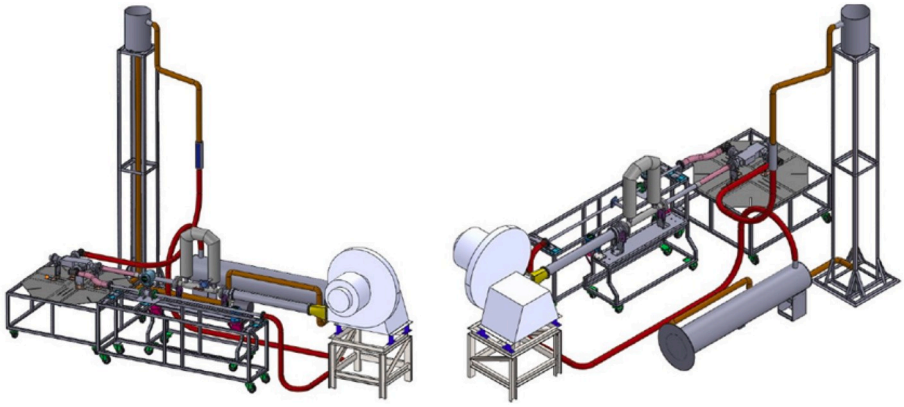

Fig. 6. CAD model of the experimental setup.

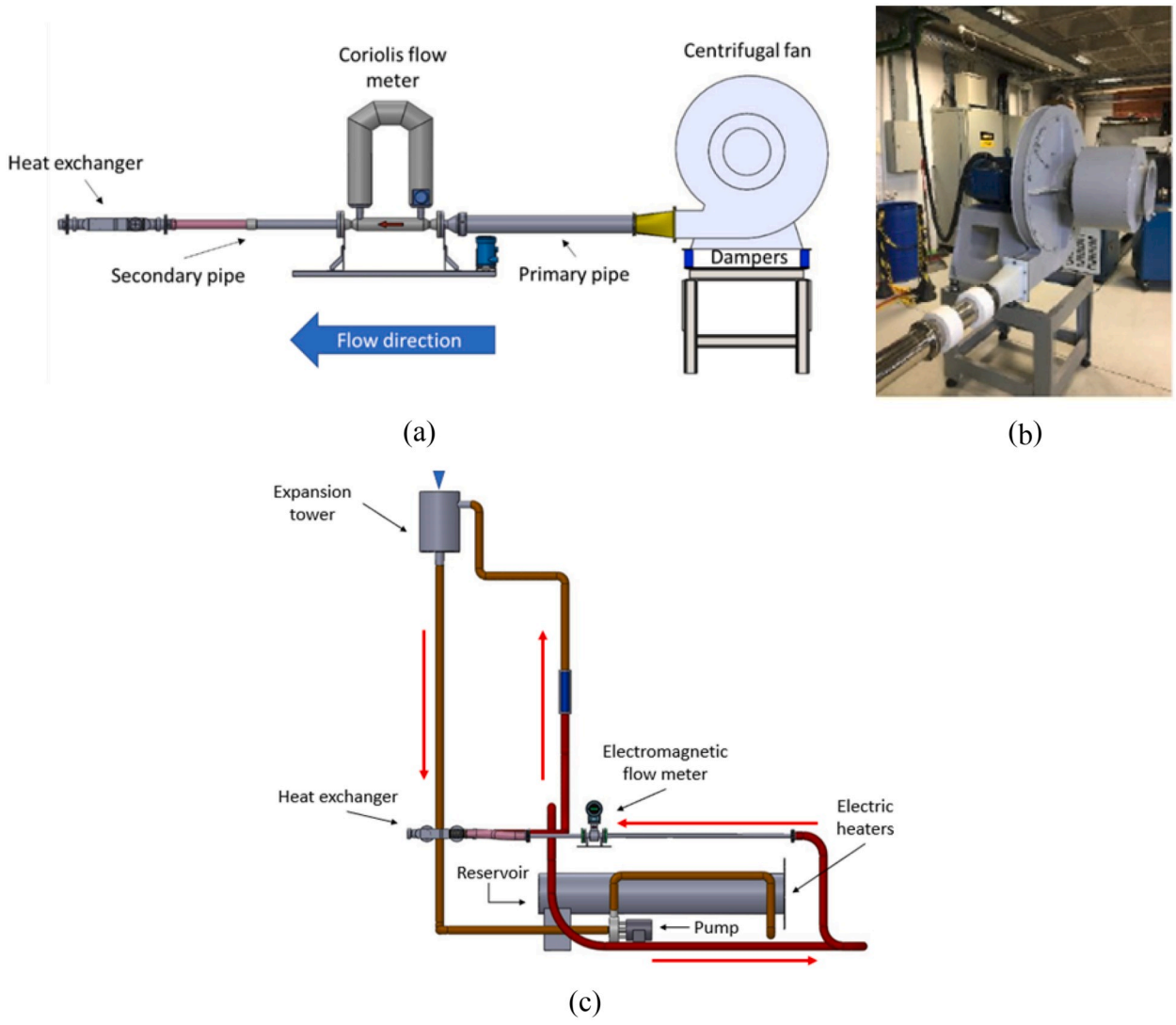

Fig. 7. (a) Cold branch CAD model. (b) High-power fan. (c) Hot branch.

Several T-type thermocouples located on the external heat exchanger wall with an accuracy of ±1 °C. Fig. 8 shows the testing section and Table 2 relates positioning and measurement instruments.

A potentiometer is used to control de centrifugal fan power input and so its velocity. A proportional-integral-derivative (PID) controller adjusts the electrical heater power inputs; a data acquisition equipment (National Instrument™ NI cDAQ-9178) acquires the data that is stored in a desktop provided with a real-time processing software (NI LabVIEW).

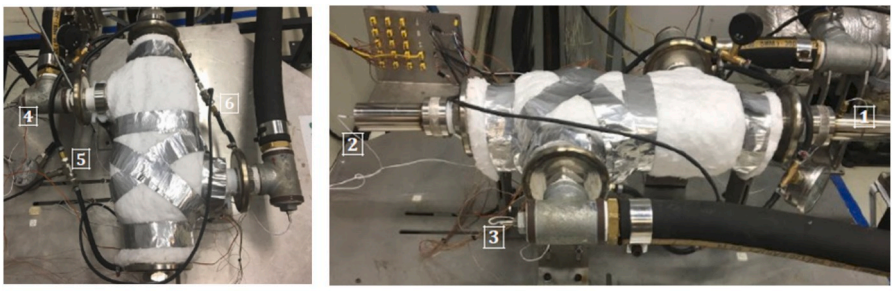

Fig. 8. (a) Top view. (b) Side view of the testing section.

Table 2
Measuring equipment position in the testing section.

Position	Measuring instruments
1	Cold branch inlet RTD
2	Cold branch outlet RTD
3	Hot branch inlet RTD
4	Hot branch outlet RTD
5	Cold branch pressure transducer
6	Hot branch pressure transducer

3.3. Experimental procedure and test combination

The compact heat exchanger was tested in several conditions. The hot stream was submitted to two temperatures, 70 °C and 80 °C, and two mass flow rates, 0.90 kg/s and 1.35 kg/s. For each temperature and mass flow rate combination of the hot branch, the centerline flow velocity of the cold branch was varied from 3.5 m/s to 12.0 m/s, with increments of 0.5 m/s. Note that the compact heat exchanger was tested from the minimum to maximum fan capacity. Therefore, 72 tests within the transition and the turbulent regimes were performed in total. Table 3 shows all the performed test. Each testing conditions took approximately 45 min to guarantee steady-state conditions, considered achieved when temperature variations on the external walls were less than the thermocouple uncertainty. After the steady-state regime was achieved, 300 measurements were taken for all the sensors for each test configuration and the steady-state temperature was taken from the average of these temperature readings.

The heat transferred through the heat exchanger are usually determined using two different mathematical methods: the logarithmic mean temperature difference (LMTD) and the number of transfer units (NTU). Considering that all the inlets and outlets temperatures were experimentally obtained, the LMTD is more convenient to be applied in this work. The overall thermal conductance of counterflow heat exchangers can be calculated as:

$$\mathrm{UA}_{\mathrm{exp}} = \frac{q_{\mathrm{exp}}}{\Delta T_{\mathrm{LM}}} \tag{29}$$

where,

$$\Delta T_{\mathrm{LM}} = \frac{\Delta T_A - \Delta T_B}{\ln\left(\frac{\Delta T_A}{\Delta T_B}\right)} \tag{30}$$

in addition, where ΔT_A and ΔT_B differences are given by,

$$\Delta T_A = T_{\mathrm{hot,in}} - T_{\mathrm{cold,out}} \tag{31}$$

$$\Delta T_B = T_{\mathrm{hot,out}} - T_{\mathrm{cold,in}} \tag{32}$$

the subscripts *hot* and *cold* are related to the hot and cold branches, respectively. Therefore, the heat rate for each stream, q_{exp}, can be determined from:

$$\begin{aligned} q_{\mathrm{hot,exp}} &= \dot{m}_{\mathrm{hot}} \bar{c}_{p,\mathrm{hot}} (T_{\mathrm{hot,in}} - T_{\mathrm{hot,out}}) = C_{\mathrm{hot}} \Delta T_{\mathrm{hot}} q_{\mathrm{cold,exp}} \\ &= \dot{m}_{\mathrm{cold}} \ \bar{c}_{p,\mathrm{cold}} (T_{\mathrm{cold,out}} - T_{\mathrm{cold,in}}) = C_{\mathrm{cold}} \Delta T_{\mathrm{cold}} \end{aligned} \tag{33}$$

where $\dot{m}_{\mathrm{cold}}$ and $\dot{m}_{\mathrm{hot}}$ were experimentally measured by the Coriolis and the electromagnetic flowmeter, respectively, the inlet and outlet temperatures of the streams were obtained from the RTDs and the specific heat capacity, $\bar{c}_p$, was evaluated at the average temperature for both cold and hot branches given by:

$$T_{\mathrm{average,cold}} = \frac{T_{\mathrm{cold,out}} + T_{\mathrm{cold,in}}}{2} \, T_{\mathrm{average,hot}} = \frac{T_{\mathrm{hot,out}} + T_{\mathrm{hot,in}}}{2} \tag{34}$$

An uncertainty analysis was conducted to find the error propagation from the measurements according to the method presented in [41]. Typical uncertainties for the parameters considered in the results are listed in Table 4. Appendix A presents in more detail the procedure for estimating the uncertainty parameters of the variables.

4. Results and discussion

4.1. Experimental results

Following the procedure described in the last section, it was possible to obtain the experimental heat transfer and the overall thermal conductance of the tested heat exchanger. They are shown as a function of Reynolds number in Fig. 9a and Fig. 9c. Fig. 9b shows the heat transfer rate balance between air and water streams. The legends refer to the hot stream and air velocity conditions, for example, 70090035 stands for water at 70 °C, mass flow rate of 0.90 kg/s and air velocity of 3.5 m/s. All experimental uncertainties were calculated but the error bars were omitted in Fig. 9 to avoid information overload.

It is important to observe that although the cold stream velocity is the only parameter directly varied during each battery of tests, it was observed, during the experiments, a linear increase of the inlet temperature of the cold fluid stream, from approximatively 25 °C–50 °C. This temperature rise can be explained by the heating of the centrifugal fan, which caused the inlet air to increase slowly during its operation. As a consequence, as observed in Fig. 9a, the heat transfer rate on the cold fluid decreased with the increase of the Reynolds number. This behavior is observed especially for test a (70090035–70090120) and b (70135035–70135120) with Reynolds number larger than 4000.

As observed in Fig. 9b, the heat transfer rate values calculated in the cold stream are large than the heat transfer values in the hot stream. This is due to the measurement uncertainty of ΔT, which in the case of the water is very small because of its large specific heat. Sometimes the measured ΔT was less than the experimental error. Therefore, we employed the heat transfer data calculated in the air side only, where the temperature gradient (between the inlet and outlet) is much larger than the measurement uncertainty. Since all heat is transferred from the water to the air, the heat transfer rates should be nearly identical apart from the heat losses. According to the technical standards [42], heat

Table 3
Experimental test performed.

Test	Air centerline velocity, m/s	Cold mass flow rate, kg/s	Hot mass flow rate, kg/s	Hot inlet temperature, °C	Cold inlet temperature, °C	Hot outlet temperature, °C	Cold outlet temperature, °C
70090035	3.5	0.0272	0.893	69.49	27.65	69.25	64.49
70090040	4.0	0.0308	0.894	69.69	29.94	69.42	65.13
70090045	4.5	0.0334	0.895	69.77	30.44	69.48	65.15
70090050	5.0	0.0366	0.894	69.68	31.16	69.36	64.96
70090055	5.5	0.0396	0.894	69.72	32.23	69.41	65.03
70090060	6.0	0.0435	0.89	69.69	29.88	69.32	64.58
70090065	6.5	0.046	0.899	69.74	33.08	69.38	64.91
70090070	7.0	0.0489	0.891	69.71	32.55	69.30	64.64
70090075	7.5	0.0518	0.899	69.82	35.72	69.43	65.07
70090080	8.0	0.0551	0.893	69.52	31.93	69.07	64.20
70090085	8.5	0.0574	0.895	69.73	35.99	69.32	64.88
70090090	9.0	0.0623	0.890	69.43	34.53	68.97	64.27
70090095	9.5	0.0648	0.898	69.70	35.64	69.24	64.52
70090100	10.0	0.0672	0.890	69.46	37.85	68.98	64.60
70090105	10.5	0.0699	0.895	69.99	37.78	69.49	64.87
70090110	11.0	0.0719	0.889	69.69	40.43	69.22	65.01
70090115	11.5	0.0749	0.895	69.59	40.30	69.10	64.80
70090120	12.0	0.0795	0.887	69.68	44.53	69.19	65.40
70135035	3.5	0.029	1.354	69.56	24.97	69.38	64.51
70135040	4.0	0.0315	1.360	69.55	25.52	69.35	64.60
70135045	4.5	0.0345	1.372	69.6	26.41	69.39	64.59
70135050	5.0	0.0377	1.358	69.42	27.40	69.20	64.38
70135055	5.5	0.0409	1.372	69.73	28.30	69.50	64.61
70135060	6.0	0.0433	1.358	69.56	29.81	69.31	64.55
70135065	6.5	0.0463	1.370	69.47	33.28	69.23	64.82
70135070	7.0	0.0484	1.356	69.43	36.05	69.19	65.07
70135075	7.5	0.0518	1.364	69.56	35.80	69.30	65.03
70135080	8.0	0.0541	1.356	69.35	35.09	69.07	64.70
70135085	8.5	0.0575	1.357	69.57	35.86	69.29	64.84
70135090	9.0	0.061	1.358	69.37	36.67	69.06	64.67
70135095	9.5	0.0633	1.360	69.37	38.19	69.07	64.82
70135100	10.0	0.0667	1.362	69.46	39.33	69.16	64.97
70135105	10.5	0.069	1.362	69.57	40.37	69.26	65.14
70135110	11.0	0.0715	1.362	69.52	41.57	69.21	65.22
70135115	11.5	0.0739	1.361	69.62	42.61	69.31	65.40
70135120	12.0	0.0798	1.361	69.61	46.03	69.31	65.78
80090035	3.5	0.0287	0.9136	79.56	26.49	79.22	73.25
80090040	4.0	0.0314	0.9187	79.49	27.45	79.15	73.45
80090045	4.5	0.0347	0.9196	80.02	26.97	79.63	73.63
80090050	5.0	0.0374	0.9052	79.61	30.19	79.22	73.63
80090055	5.5	0.0403	0.9047	79.50	31.25	79.09	73.44
80090060	6.0	0.0433	0.9162	79.35	31.23	78.92	73.19
80090065	6.5	0.046	0.9129	79.71	32.22	79.23	73.34
80090070	7.0	0.0481	0.9168	79.59	35.29	79.13	73.62
80090075	7.5	0.0509	0.9166	79.45	36.25	79.01	73.62
80090080	8.0	0.054	0.8938	79.38	35.12	78.84	73.15
80090085	8.5	0.058	0.8844	79.27	36.55	78.70	73.07
80090090	9.0	0.0617	0.9121	79.75	36.53	79.16	73.31
80090095	9.5	0.064	0.9029	79.40	37.88	78.83	73.18
80090100	10.0	0.0666	0.8928	79.53	38.99	78.96	73.36
80090105	10.5	0.069	0.8856	79.68	39.80	79.05	73.39
80090110	11.0	0.0718	0.9133	79.58	40.58	78.98	73.40
80090115	11.5	0.0743	0.9131	79.76	40.91	79.15	73.53
80090120	12.0	0.0768	0.8891	79.8	42.19	79.15	73.56
80135035	3.5	0.0286	1.374	79.32	26.61	79.11	73.19
80135040	4.0	0.0314	1.370	79.41	27.41	79.17	73.52
80135045	4.5	0.0346	1.377	79.64	27.28	79.38	73.51
80135050	5.0	0.0374	1.368	79.60	30.11	79.34	73.68
80135055	5.5	0.0402	1.364	79.42	31.39	79.14	73.54
80135060	6.0	0.0433	1.378	79.38	31.28	79.07	73.33
80135065	6.5	0.0459	1.364	79.41	33.34	79.10	73.52
80135070	7.0	0.0482	1.368	79.43	35.15	79.11	73.66
80135075	7.5	0.0508	1.369	79.28	36.52	78.96	73.61
80135080	8.0	0.0541	1.366	79.25	34.46	78.89	73.17
80135085	8.5	0.0579	1.374	79.27	36.63	78.91	73.32
80135090	9.0	0.0616	1.380	79.36	36.79	78.98	73.25
80135095	9.5	0.064	1.367	79.38	37.70	78.99	73.31
80135100	10.0	0.0665	1.363	79.35	38.97	78.95	73.35
80135105	10.5	0.0691	1.359	79.31	39.75	78.91	73.36
80135110	11.0	0.0718	1.377	79.39	40.56	78.98	73.44
80135115	11.5	0.0743	1.358	79.56	41.09	79.13	73.55
80135120	12.0	0.0767	1.320	79.43	42.36	79.00	73.54

Table 4
Experimental errors.

Parameter	Uncertainties
Heat transfer rate	8.5–35.5 W
Inlet/outlet temperature	±0.1–0.27 °C
Overall thermal conductance	±5%
Mass flow rate cold side	±0.26–0.5%

losses or measurement errors cannot be larger than 10%. Also, as observed in published papers, when dealing with diffusion-bonded heat exchangers, the heat unbalance can be as high as 7% [13,16,28,43] and the heat loss ratio can be as high as 19% [44].

As shown in Fig. 1, the heat exchanger operates in a counter-flow configuration. However, to separate the fluids at the ends of the heat exchanger and to install headers, it is necessary to provide a cross-flow region. As a result, a composite heat exchanger with a pure counter-flow central region, but with cross-flow near the headers is obtained. As presented by Kays et al. [45] the performance, based on the total heat transfer surface area, would be inferior to that of a simple counter-flow arrangement, but superior to a simple cross-flow arrangement. In addition, the effect of the cross-flow at the inlet and outlet headers on the effectiveness of the heat exchanger decreases for a longer heat exchanger length [45,46]. Therefore, it is necessary to establish an effective heat exchanger length. Three characteristic lengths can be used, namely, the L_{hot}, L_{cold} and $L_{pure\ counter\text{-}flow}$ to calculate the thermal performance of the compact heat exchanger.

Fig. 9d shows the effect of the characteristic length on the calculation of the thermal conductance of the heat exchanger. Note that the hot stream length, L_{hot}, was the effective heat transfer lengths, i.e., it was discounted the entrance and outlet length on the total hot side length. As one can note, the use of L_{med} which is an intermediate value between the hot L_{hot} and cold L_{cold} lengths as input data for the model results in good comparison with the experimental conductance, calculated by Equation (29). When the pure counter-flow length is used as the effective length, the results diverge largely to the experimental data, showing the importance of the cross-flow heat transfer at the headers on the performance of the heat exchanger. L_{med} is used as the effective length in the next sections, as heat transfer parameter presents the smallest RSME when compared to experimental data.

4.2. Flow maldistribution numerical analysis

As described in section 2.1, the fluid is considered uniformly distributed among the channels with a uniform velocity profile at the inlet channels. However, this hypothesis may not be realistic. To define the degree of flow maldistribution, Baek et al. [47] developed a coefficient of variation, CoV parameter, which varies from 0 to very large positive values, where zero indicates the ideally distributed flow condition. CoV is expressed as:

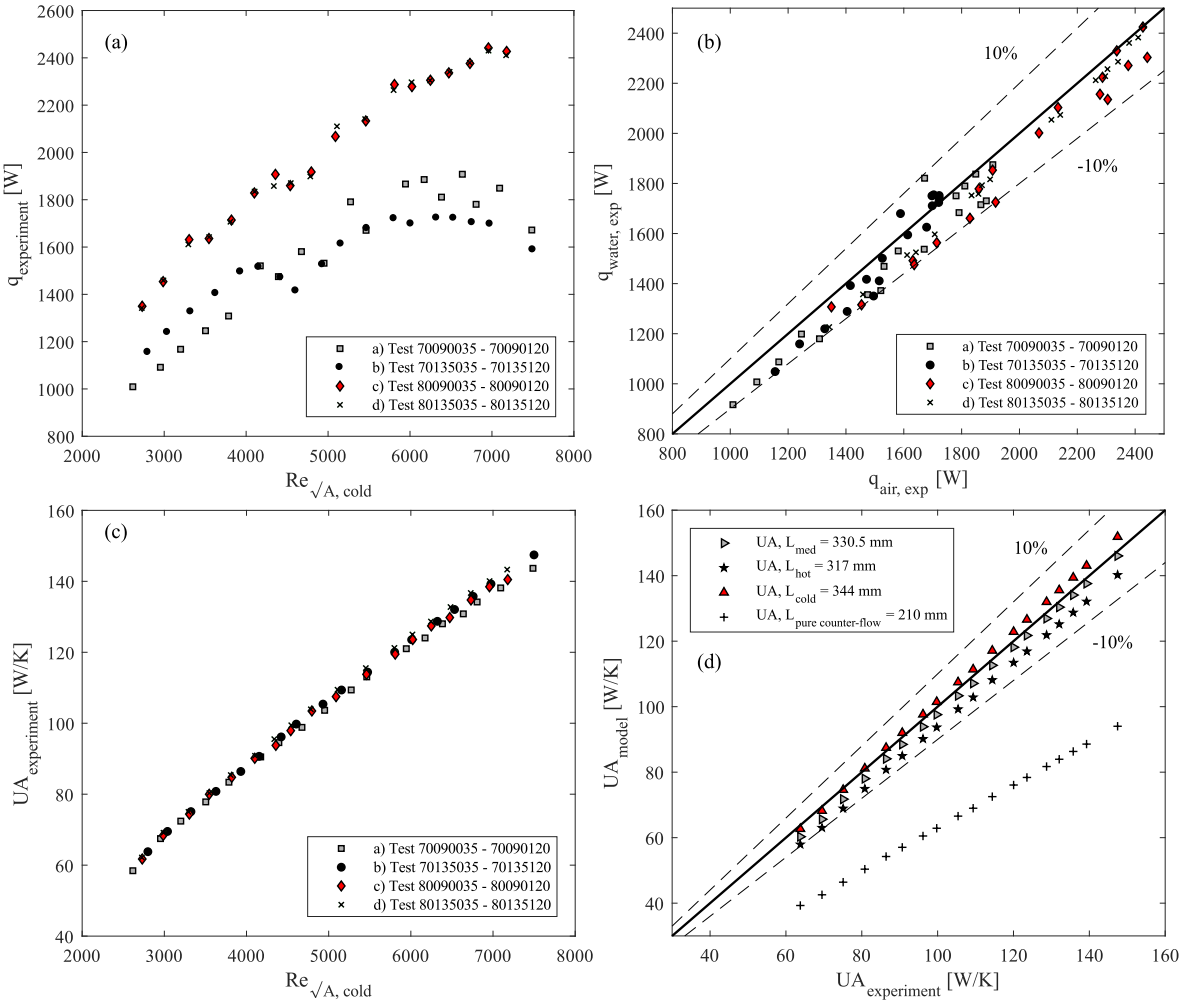

Fig. 9. Experimental results for (a) Heat rate. (b) Heat balance between air and water. (c) Thermal conductance. (d) Characteristic length of the heat exchanger. Experimental data from Test 70135035–70135120.

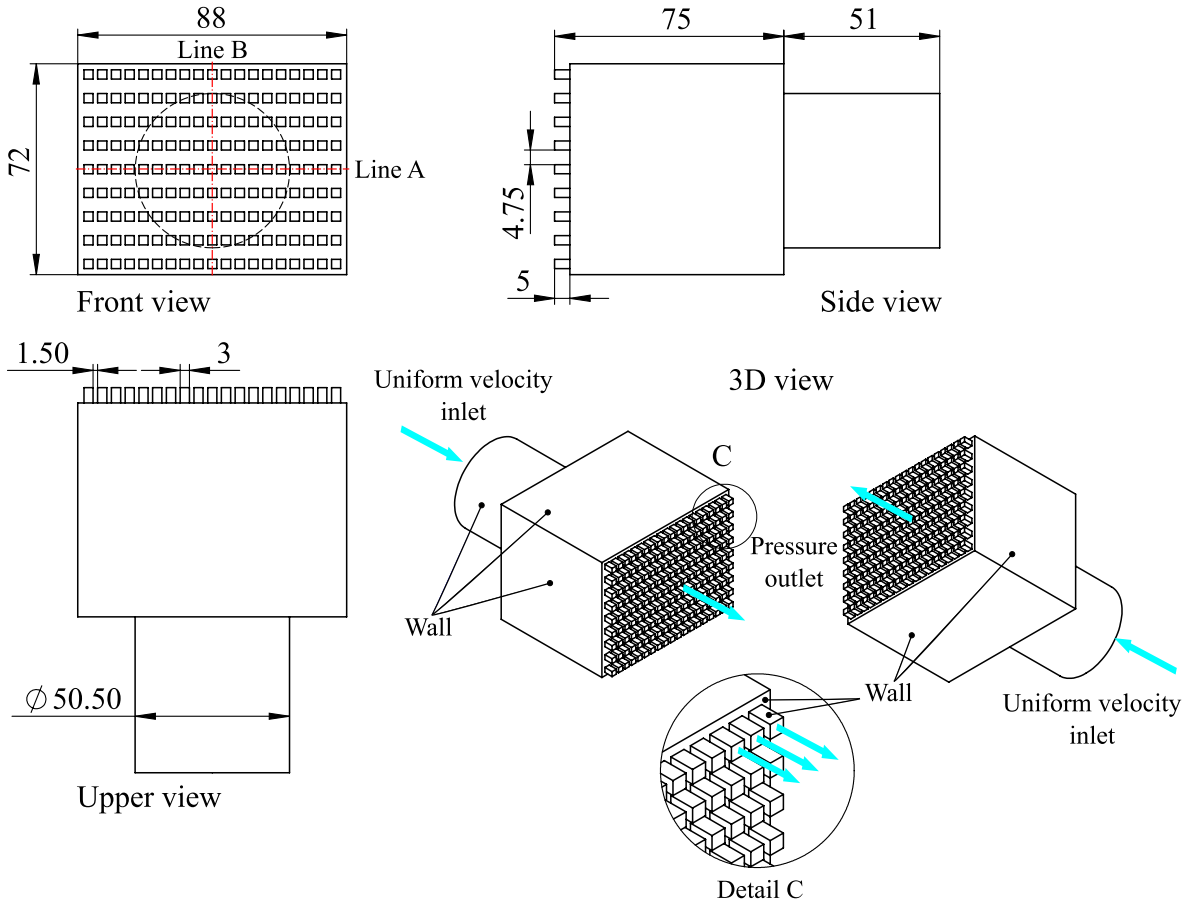

Fig. 10. 3D model of the header. Only the fluid domain is shown. All dimensions are in millimeters.

$$\mathrm{CoV} = \frac{\text{strandard deviation}}{\text{average}} = \frac{\sqrt{\frac{\sum_{i=1}^{N}(\dot{m}_i - \overline{m})^2}{M}}}{\overline{m}} \tag{35}$$

where $\dot{m}_i$ is the actual mass flow rate for the i channel, $\overline{m}$ is the average mass flow rate and M is the total number of channels.

Due to the difficulties associated to measuring the mass flow rate for each channel and to establish if the hypothesis is valid or not, a full 3D numerical simulation was developed. The software ANSYS – CFX v19.2 was used in this study. Through this simulation it is possible to estimate the mass flow rate for all channels and mass flow distribution in each channel. Fig. 10 left side shows the numerical domain of the inlet header and the boundary conditions. The inlet and outlet headers for cold and hot sides are exactly the same, where the dimensions are also presented in Fig. 10. Details of this simulation are presented in this section.

The differential equations of mass conservation and momentum were discretized by the finite volume method and solved in an iterative process [48]. The following hypotheses are adopted: multidimensional and incompressible flow, constant physical properties, no internal heat generation, no radiation heat transfer, and no buoyancy effects. Therefore, the mass conservation equation is:

$$\frac{\partial \rho}{\partial t} + \frac{\partial}{\partial x_j}(\rho u_j) = 0 \tag{36}$$

while the momentum conservation equation is written as:

$$\frac{\partial \rho}{\partial t} + \frac{\partial}{\partial x_j}(\rho u_j u_i) = -\frac{\partial p}{\partial x_i} + \frac{\partial}{\partial x_j}\left(\mu \frac{\partial u_i}{\partial x_j}\right) + \mathbf{F} \tag{37}$$

where x_j are cartesian components (x, y, z), u_j are velocity components (u, v, w) and $\mathbf{F}$ are volume field forces. For the turbulent regime, the standard k - ε_f turbulence model, which belongs to the Reynolds Average Navier-Stokes Equations (RANS) class, was used. This is a semi-empirical model, based on the diffusion gradient hypothesis that is used to relate the Reynolds tensor with the average velocity gradient and the turbulent viscosity. Turbulence kinetic energy k is related to the variations of velocities and ε_f is the fluctuation dissipation rate of k. For k, the following expression is valid:

$$\frac{\partial}{\partial t}(\rho k) + \frac{\partial}{\partial x_j}(\rho u_j k) = \frac{\partial}{\partial x_j}\left[\left(\mu + \frac{\mu_t}{\sigma_k}\right)\frac{\partial k}{\partial x_j}\right] + P_k - \rho\varepsilon_f + P_{kb} \tag{38}$$

while for ε:

$$\frac{\partial}{\partial t}(\rho\varepsilon_f) + \frac{\partial}{\partial x_j}(\rho u_j \varepsilon_f) = \frac{\partial}{\partial x_j}\left[\left(\mu + \frac{\mu_t}{\sigma_\varepsilon}\right)\frac{\partial \varepsilon_f}{\partial x_j}\right] + \frac{\varepsilon_f}{k}\left(C_{1\varepsilon}P_k - C_{2\varepsilon}\rho\varepsilon_f + C_{1\varepsilon}P_{\varepsilon b}\right) \tag{39}$$

where turbulent viscosity term is defined as $\mu_t = \rho C_\mu k^2/\varepsilon_f$ and $C_{1\varepsilon f} = 1.44$, $C_{2\,\varepsilon f} = 1.92$, $C_\mu = 0.09$ and $\sigma_{\varepsilon f} = 1.3$ are takes as constants. P_{kb} and P_b represent the buoyancy forces influence and P_k is turbulence production, due to viscous forces [49]. For wall treatment, a scalable wall function was used.

To solve the differential equations, the next assumptions were made: constant mass flow rate at the inlet of the header with uniform velocity profile, no heat transfer across the walls (adiabatic condition) and no-slip condition on the header and channel walls. The CFD boundary conditions used in the simulation are presented in Fig. 10. The convergence criteria in the order of 10^{-7} were established for the mean square (RMS) error, for the discretized forms of Equations (36)–(39).

To establish the influence of mesh size on the results of the simulation, three numerical simulations were developed. Hexahedral meshes

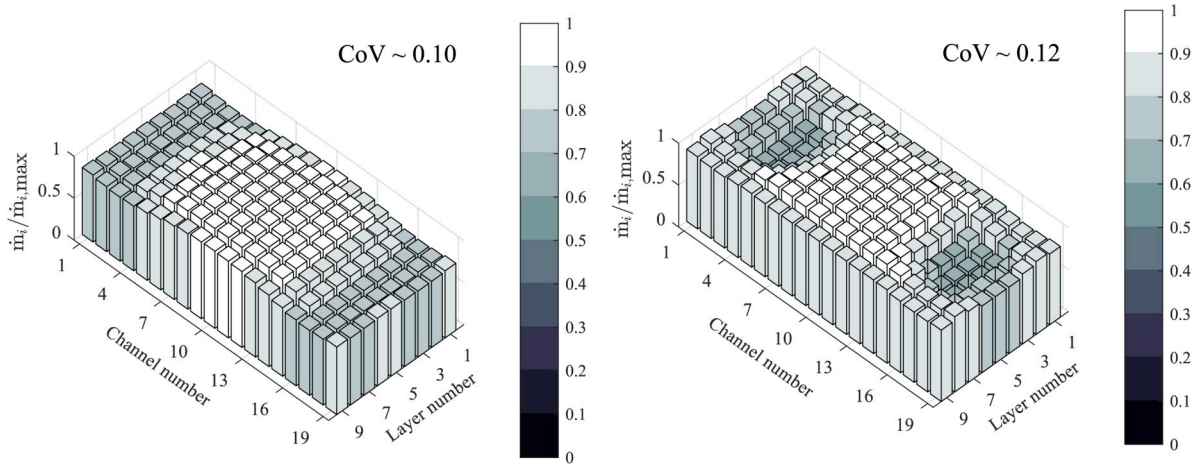

Fig. 11. Mass flow distribution for both cold and hot inlet headers.

were used with an orthogonal quality near to one. Mesh dependency analysis was performed based on the maximum mass flow rate at the inlet header. The number of elements considered varied from 1.5×10^6 to 4.5×10^6 for the first and third simulations, respectively. It was observed that the mass flow distribution obtained using 2.5×10^6 and 4.5×10^6 elements is almost the same, with a maximum difference of approximately 3%, considering all channels. Therefore, a mesh with 2.5×10^6 elements was chosen. After the mesh dependence analysis, the data for mass flow rate for each channel was obtained and, using Equation (35), the coefficient of variation was calculated.

Fig. 11 shows the numerical results for the mass flow rate distribution of both cold and hot fluid in the inlet headers. Note that the mass flow rate (see bars in Fig. 11) was non-dimensionalized by the maximum mass flow rate. Note that a there is a recirculation flow in the header, and it is account for by the conservation equations. However, once the fluid enters the heat exchanger, there is no mixture between channels. Therefore a value of $\dot{m}_i/\dot{m}_{i,\max} = 1$ is observed at channel number 10 and layer number 5. The simulated cold and hot headers have a CoV of around 0.10 and 0.12, respectively, which means that an almost homogeneous mass flow rate distribution was predicted.

As shown by Baek et al. [47], the thermal performance of compact heat exchangers is almost not affected by the maldistribution mass flow on the channels, if CoV and the axial parameter conduction are less than 0.15 and 0.001, respectively, for the laminar regime. Note that the thermal performance degradation is intensified when the heat exchanger has more channels, the inlet header presents large aspect ratio (the diameter of the inlet tube is small when compared with the height and/or width of the header) and, the effect of the axial conduction is large. As observed by Baek et al. [47] for the same inlet temperature, the outlet temperature of a heat exchanger can be estimated by the weighted average of temperature and mass flow rates of each channel. For the case of heat exchangers with high CoV, the fluid outlet temperature is mostly dominated by the channels with larger mass flow rates. However, for heat exchangers with a homogeneous mass flow distribution (low CoV value), the fluid outlet temperature is determined by channels with an average mass flow rate.

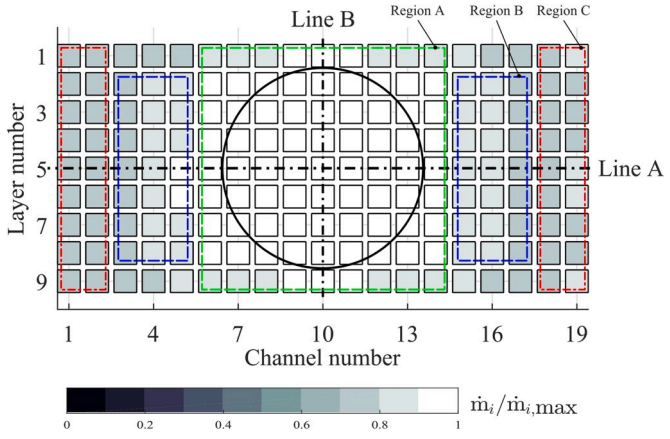

Fig. 12. Mass flow distribution zones at cold inlet header.

Fig. 12 presents mass flow rate distribution zones where one can identify three regions defined according to the value of $\dot{m}_i/\dot{m}_{i,\max}$. For the zone near the fluid inlet jet influence (region A), an almost homogeneous mass flow rate distribution can be observed, with low CoV values ($\dot{m}_i/\dot{m}_{i,\max} \cong 1$). In the region B, a slight reduction in the mass flow rate can be observed. This phenomenon is due to recirculation effects and the value of $\dot{m}_i/\dot{m}_{i,\max}$ is between approximately 0.85 and 0.95. The region far from the inlet jet influence (region C) experiments a reduction of mass flow rate due to the larger distance from inlet jet ($\dot{m}_i/\dot{m}_{i,\max} \cong 0.75$). The values of $\dot{m}_i/\dot{m}_{i,\max}$ for the zones B and C can vary depending on the relation between the jet diameter and the aspect relation of the header, as stated above. The vertical flow distribution, line B, shows fairly ideal distribution, however, the horizontal distribution (line A) shows a center-weighted distribution.

4.3. Comparison between the proposed model and heat exchanger experimental data

Based on the set of equations and procedures described in section 2, a theoretical model was used to predict the thermal performance of the compact heat exchanger. This model was implemented in the software MATLAB®. The heat transfer coefficient obtained from literature expressions for the Nusselt number (Gnielinksi [14,32], Taler [37] and Sarmiento et al. [38]) were used for the estimative of the convection heat transfer coefficient in the thermal model. The resulted curves are compared with experimental data in this section. Note that all the Nusselt models have been converted to the same characteristic length scale, $\sqrt{A}$, as proposed by Sarmiento et al. [38].

Fig. 13 shows the thermal conductance as a function of Reynolds number for all the experimental data obtained from the experimental setup. Fig. 13a presents the results for UA for the set of tests 70090035–70090120. Note that, as presented in Table 3, there is a little variation on the mass flow rate for the hot stream, which no represent expressive variations on Reynolds number. Therefore, $\mathrm{Re}_{\sqrt{A},\mathrm{hot}}$ can be considered almost constant in the hot stream, while the mass flow in the cold stream varies from the lowest 70090035 to the highest 70090120 values. Also, the three theoretical curves, based on literature correlations (Gnielinksi [14,32], Taler [37] and Sarmiento et al. [38]), are

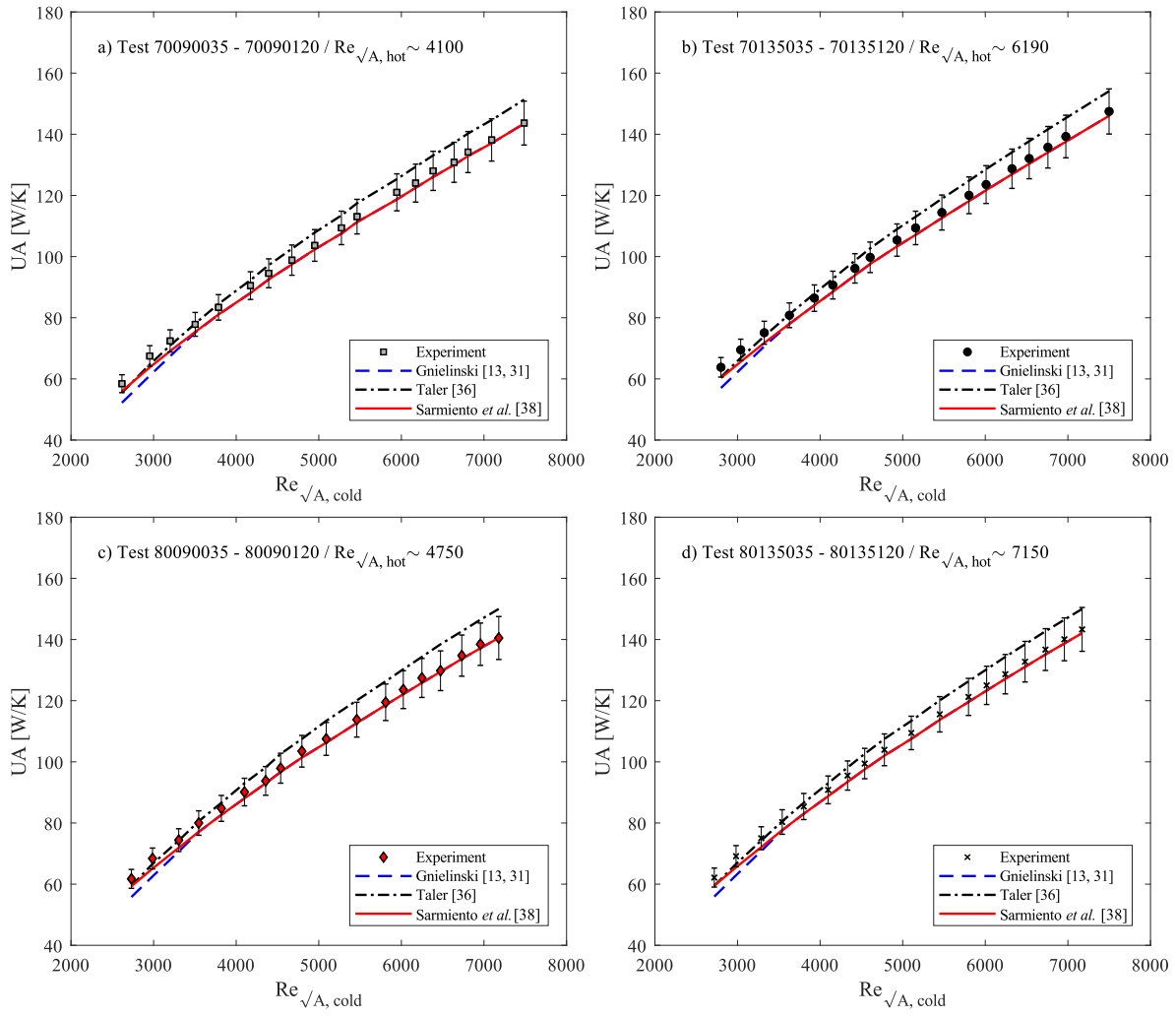

Fig. 13. Comparison between experimental values of UA with the predicted ones using the correlations of Gnielinksi [14,32], Taler [37] and Sarmiento et al. [38].

compared with data.

Fig. 13b, c and d show similar plots to the one presented in Fig. 13a. In the case of Fig. 13b, the hot stream mass flow rate was kept constant at the highest value, while the mass flow in the cold stream varies from the lowest 70135035 to the highest 70135120 values. For the case of Fig. 13c and d, the inlet temperature of the hot stream was kept nearby 80 °C.

In general, Fig. 13a, b, c, and d, show that the theoretical models and experimental data present the same trends for the overall thermal resistance. The model proposed by Sarmiento et al. [38] presents the best comparison with data in all plots (RMSE = 2%). In all cases, these model curves are located within the data error bars. Besides, Gnielisnki and Taler models show a very close estimative when compared with all the experimental data with RMSE equal to 2.7% and 4%, respectively. Note that for the data, which Reynolds number in the cold stream ranges between 2600 and 4200, the Taler model compares with the data within 2% and 4%, respectively. This difference goes up for high Reynolds numbers, reaching a maximum of 7%. On the other hand, the Sarmiento et al. [38] model shows similar behavior to the Gnielinski model, for Reynolds numbers greater than ~3500. This behavior can be explained because Sarmiento et al. [38] used the Gnielinski model for turbulent flow in their correlation. For Reynolds number less than 3500 the linear interpolation proposed by Gnielinski shows a good agreement with the experimental data, but, as shown by Sarmiento et al. [38], for transition regimes, the linear interpolation is less accurate.

Fig. 14 shows a comparison between the theoretical predictions of

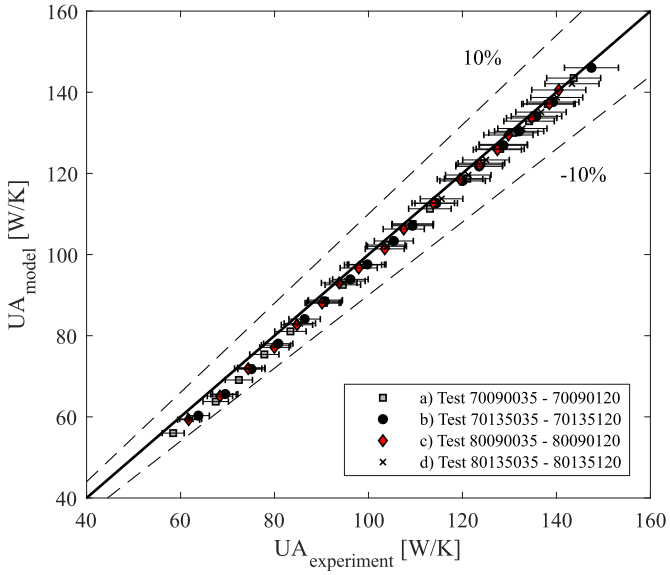

Fig. 14. Comparison between the theoretical and experimental data.

the thermal conductance calculated with Equation (11) and experimental data. The full line shows the perfect comparison, while the dashed lines define the 10% variation region around the perfect comparison line.

It is possible to observe that the model tends to underpredict the data slightly for low Reynolds numbers (small overall thermal conductance). For high Reynolds numbers, the experimental results were very close to the ideal line, showing that the model proposed by Sarmiento et al. [38] agrees very well with the experimental data.

In general, Figs. 13 and 14 show that the theoretical models and experimental data present the same trends for the thermal conductance curves. The present theoretical model, in which the heat transfer coefficient is predicted by Sarmiento et al. [38] expressions, shows the best comparison with data in all plots within the data error bars.

5. Conclusions

The focus of this paper was to study, theoretically and experimentally, a compact heat exchanger fabricated using diffusion bonding process. Based on geometrical parameters of a heat exchanger core and on fundamental heat transfer equations, an analytical model to estimate the thermal behavior was proposed. Different Nusselt numbers correlations taken from literature, for predicting the internal convection heat transfer within a compact heat exchanger, were selected as input expression for the thermal behavior model, which was applied to the analyzed equipment. The proposed model was implemented in commercial software.

A compact heat exchanger prototype, joined by diffusion bonding technique, was manufactured using water–jet cutting tools to produce the square cross-section mini-channels. The channels were formed by stacking flat and comb-like machined layers. The prototype was tested in different temperatures and mass flow rates levels, employing water and air as working fluids for hot and cold streams, respectively. The test consisted of keeping the average inlet temperature of the hot stream in two levels at approximately 70 °C and 80 °C with mass flow rates equal to 0.90 kg/s and 1.35 kg/s, meanwhile for each hot stream temperature and mass flow rate combinations, the flow velocity of the cold branch varied from 3.5 m/s to 12.0 m/s using increments of 0.5 m/s. Therefore, 72 tests were performed.

The experimental data were compared with the proposed theoretical model. It was observed that all the theoretical model curves compare well with the thermal conductance data, following the same behavior trend of the data points, and so, these models can be used to predict the thermal behavior of the compact heat exchanger in the transition regime. Also, note that the comparison between the experimental and theoretical heat transfer rates showed an excellent agreement with an RSME less than 2%. Among the employed Nusselt number correlations for convection heat transfer in minichannels, the correlation of Taler [24] presented the major difference between the theoretical and experimental results (RSME = 4%). The correlation presented by Gnielinski [8] presented an almost constant difference between the theoretical and experimental results (RSME = 2.7%). On the other hand, the correlation proposed by Sarmiento et al. [38] presented the lower difference when compared to the experimental data (RSME = 2%). The results of numerical simulations of the headers show a small value (around 0.1 and 0.12) for the coefficient of variation, CoV, which means an almost uniform mass flow distribution among the channels.

Declaration of competing interest

None.

Acknowledgments

The authors gratefully thank CAPES (Coordination for Improvement of Higher Education Personnel, Brazil), and PETROBRAS (Brazilian Petroleum Corporation, Brazil) for financial support.

Appendix A Uncertainity analysis

Appendix A Uncertainity analysis

The heat transfer for both hot and cold streams was computed by:

$$q = \dot{m} c_p (T_{out} - T_{in}) = \dot{m} c_p \Delta T \tag{40}$$

where $\dot{m}$, c_p and ΔT represent the mass flow rate, specific heat at constant pressure and the temperature difference between inlet and outlet, respectively. Considering that c_p is a well-known value $u(c_p) = 0$, the standard uncertainty for q is given by:

$$u(q) = \left[\left(\frac{\partial q}{\partial \dot{m}} u(\dot{m}) \right)^2 + \left(\frac{\partial q}{\partial \Delta T} u(\Delta T) \right)^2 \right]^{1/2} \tag{41}$$

where $u(\cdot)$ represents the standard uncertainty. The effective number of degrees of freedom for q, $\nu_{ef,q}$, is computed by:

$$\frac{\left[\frac{u(q)}{q}\right]^4}{\nu_{ef,q}} = \frac{\left[\frac{u(\dot{m})}{\dot{m}}\right]^4}{\nu_{\dot{m}}} + \frac{\left[\frac{u(\Delta T)}{\Delta T}\right]^4}{\nu_{\Delta T}} \tag{42}$$

where ν represents the number of degrees of freedom. Here, $\nu_{\Delta T}$ can be considered as infinity. The expanded uncertainty for the heat transfer rate, $U(q)$, can be written as:

$$U(q) = t \cdot u(q) \tag{43}$$

where t is determined by $\nu_{ef,q}$ for a confidence interval of 95%. The heat transfer rate measurement is then given by:

$$q = \overline{q} \pm U(q) \tag{44}$$

where $\overline{q}$ stand for the average heat transfer rate.

The thermal conductance can be calculated as shown in Equation (29):

$$\mathrm{UA} = \frac{q}{\Delta T_{\mathrm{LM}}} \tag{45}$$

Following a similar procedure described above, the uncertainty relative to the thermal conductance is given by:

$$\mathrm{u(UA)} = \left[\left(\frac{\partial \mathrm{UA}}{\partial q}u(q)\right)^2 + \left(\frac{\partial \mathrm{UA}}{\partial \Delta T_{\mathrm{LM}}}u(\Delta T_{\mathrm{LM}})\right)^2\right]^{1/2} \quad \mathrm{u(UA)} = \left[\left(\frac{1}{\Delta T_{\mathrm{LM}}}u(q)\right)^2 + \left(-\frac{q}{\Delta T_{\mathrm{LM}}^2}u(\Delta T_{\mathrm{LM}})\right)^2\right]^{1/2} \tag{46}$$

The term $u(q)$ is estimated by Equation (41). The term relative to the logarithmic mean temperature difference, $u(\Delta T_{\mathrm{LM}})$, is calculated as follows:

$$\mathrm{u}(\Delta T_{\mathrm{LM}}) = \left[\left(\frac{\partial \Delta T_{\mathrm{LM}}}{\partial \Delta T_{\mathrm{A}}}u(\Delta T_{\mathrm{A}})\right)^2 + \left(\frac{\partial \Delta T_{\mathrm{LM}}}{\partial \Delta T_{\mathrm{B}}}u(\Delta T_{\mathrm{B}})\right)^2\right]^{1/2} \frac{\partial \Delta T_{\mathrm{LM}}}{\partial \Delta T_{\mathrm{A}}} = \frac{\Delta T_{\mathrm{A}}\, ln\left(\frac{\Delta T_{\mathrm{A}}}{\Delta T_{\mathrm{B}}}\right) - \Delta T_{\mathrm{A}} + \Delta T_{\mathrm{B}}}{\Delta T_{\mathrm{A}} ln^2\left(\frac{\Delta T_{\mathrm{A}}}{\Delta T_{\mathrm{B}}}\right)} \frac{\partial \Delta T_{\mathrm{LM}}}{\partial \Delta T_{\mathrm{B}}} = \frac{-\Delta T_{\mathrm{B}}\, ln\left(\frac{\Delta T_{\mathrm{A}}}{\Delta T_{\mathrm{B}}}\right) + \Delta T_{\mathrm{A}} - \Delta T_{\mathrm{B}}}{\Delta T_{\mathrm{B}} ln^2\left(\frac{\Delta T_{\mathrm{A}}}{\Delta T_{\mathrm{B}}}\right)} \tag{47}$$

where $u(\cdot)$ represents the standard uncertainty. The effective number of degrees of freedom for UA, $\nu_{\mathrm{ef,UA}}$, is computed by:

$$\frac{\left[\frac{u(\mathrm{UA})}{\mathrm{UA}}\right]^4}{\nu_{\mathrm{ef,UA}}} = \frac{\left[\frac{u(q)}{q}\right]^4}{\nu_q} + \frac{\left[\frac{u(\Delta T_{\mathrm{LM}})}{\Delta T_{\mathrm{LM}}}\right]^4}{\nu_{\Delta T_{\mathrm{LM}}}} \tag{48}$$

where ν represents the number of degrees of freedom. The expanded uncertainty for the heat transfer rate, U(UA), can be written as:

$$U(\mathrm{UA}) = t \cdot u(\mathrm{UA}) \tag{49}$$

where t is determined by $\nu_{\mathrm{ef,UA}}$ for a confidence interval of 95%. The heat transfer rate measurement is then given by:

$$\mathrm{UA} = \overline{\mathrm{UA}} \pm U(\mathrm{UA}) \tag{50}$$

where $\overline{\mathrm{UA}}$ stand for the average overall thermal conductance.

Appendix B. Supplementary data

Supplementary data to this article can be found online at https://doi.org/10.1016/j.ijthermalsci.2020.106384.

References

[1] R.K. Shah, D.P. Sekulić, Fundamentals of Heat Exchanger Design, John Wiley & Sons, Hoboken, NJ, 2003.

[2] A.P.C. Sarmiento, F.H. Milanese, M.B.H. Mantelli, V.R. Miranda, Theoretical and experimental studies on two-phase thermosyphon shell and shell heat exchangers, Appl. Therm. Eng. 171 (2020) 115092, https://doi.org/10.1016/j.applthermaleng.2020.115092.

[3] J.E. Hesselgreaves, R. Law, D. Reay, Compact Heat Exchangers: Selection, Design, and Operation, second ed., Butterworh-Heinemann, Amsterdam, 2017.

[4] T. Takeda, K. Kunitomi, T. Horie, K. Iwata, Feasibility study on the applicability of a diffusion-welded compact intermediate heat exchanger to next-generation high temperature gas-cooled reactor, Nucl. Eng. Des. 168 (1997) 11–21, https://doi.org/10.1016/S0029-5493(96)01361-1.

[5] M.V.V. Mortean, L.H.R. Cisterna, K.V. Paiva, M.B.H. Mantelli, Development of diffusion welded compact heat exchanger technology, Appl. Therm. Eng. 93 (2016) 995–1005, https://doi.org/10.1016/j.applthermaleng.2015.09.021.

[6] M.V.V. Mortean, A.J. de A. Buschinelli, K.V. de Paiva, M.B.H. Mantelli, J. Remmel, Soldagem por Difusão de Aços Inoxidáveis para Fabricação de Trocadores de Calor Compactos, Soldag. Insp. 21 (2016) 103–114, https://doi.org/10.1590/0104-9224/SI2101.10.

[7] M.V.V. Mortean, K.V. Paiva, M.B.H. Mantelli, Diffusion bonded cross-flow compact heat exchangers: theoretical predictions and experiments, Int. J. Therm. Sci. 110 (2016) 285–298, https://doi.org/10.1016/j.ijthermalsci.2016.07.010.

[8] N. Bartel, M. Chen, V.P. Utgikar, X. Sun, I.-H. Kim, R. Christensen, P. Sabharwall, Comparative analysis of compact heat exchangers for application as the intermediate heat exchanger for advanced nuclear reactors, Ann. Nucl. Energy 81 (2015) 143–149, https://doi.org/10.1016/j.anucene.2015.03.029.

[9] Y. Hou, G. Tang, Thermal-hydraulic-structural analysis and design optimization for micron-sized printed circuit heat exchanger, J. Therm. Sci. 28 (2019) 252–261, https://doi.org/10.1007/s11630-018-1062-8.

[10] C. Huang, W. Cai, Y. Wang, Y. Liu, Q. Li, B. Li, Review on the characteristics of flow and heat transfer in printed circuit heat exchangers, Appl. Therm. Eng. 153 (2019) 190–205, https://doi.org/10.1016/j.applthermaleng.2019.02.131.

[11] S.K. Mylavarapu, X. Sun, R.E. Glosup, R.N. Christensen, M.W. Patterson, Thermal hydraulic performance testing of printed circuit heat exchangers in a high-temperature helium test facility, Appl. Therm. Eng. 65 (2014) 605–614, https://doi.org/10.1016/j.applthermaleng.2014.01.025.

[12] J.-W. Seo, Y.-H. Kim, D. Kim, Y.-D. Choi, K.-J. Lee, Heat transfer and pressure drop characteristics in straight microchannel of printed circuit heat exchangers, Entropy 17 (2015) 3438–3457, https://doi.org/10.3390/e17053438.

[13] D. Kwon, L. Jin, W. Jung, S. Jeong, Experimental investigation of heat transfer coefficient of mini-channel PCHE (printed circuit heat exchanger), Cryogenics 92 (2018) 41–49, https://doi.org/10.1016/j.cryogenics.2018.03.011.

[14] V. Gnielinski, On heat transfer in tubes, Int. J. Heat Mass Transf. 63 (2013) 134–140, https://doi.org/10.1016/j.ijheatmasstransfer.2013.04.015.

[15] X.F. Peng, G.P. Peterson, Convective heat transfer and flow friction for water flow in microchannel structures, Int. J. Heat Mass Transf. 39 (1996) 2599–2608, https://doi.org/10.1016/0017-9310(95)00327-4.

[16] W. Chu, X. Li, T. Ma, Y. Chen, Q. Wang, Experimental investigation on SCO 2 -water heat transfer characteristics in a printed circuit heat exchanger with straight channels, Int. J. Heat Mass Transf. 113 (2017) 184–194, https://doi.org/10.1016/j.ijheatmasstransfer.2017.05.059.

[17] M.V.V. Mortean, L.H.R. Cisterna, K.V. Paiva, M.B.H. Mantelli, Thermal and hydrodynamic analysis of a cross-flow compact heat exchanger, Appl. Therm. Eng. 150 (2019) 750–761, https://doi.org/10.1016/j.applthermaleng.2019.01.038.

[18] M.V.V. Mortean, M.B.H. Mantelli, Nusselt number correlation for compact heat exchangers in transition regimes, Appl. Therm. Eng. 151 (2019) 514–522, https://doi.org/10.1016/j.applthermaleng.2019.02.017.

[19] J. Khalesi, N. Sarunac, Numerical analysis of flow and conjugate heat transfer for supercritical CO2 and liquid sodium in square microchannels, Int. J. Heat Mass Transf. 132 (2019) 1187–1199, https://doi.org/10.1016/j.ijheatmasstransfer.2018.12.071.

[20] K. Nikitin, Y. Kato, L. Ngo, Printed circuit heat exchanger thermal–hydraulic performance in supercritical CO2 experimental loop, Int. J. Refrig. 29 (2006) 807–814, https://doi.org/10.1016/j.ijrefrig.2005.11.005.

[21] F. Pra, P. Tochon, C. Mauget, J. Fokkens, S. Willemsen, Promising designs of compact heat exchangers for modular HTRs using the Brayton cycle, Nucl. Eng. Des. 238 (2008) 3160–3173, https://doi.org/10.1016/j.nucengdes.2007.12.024.

[22] M. Chen, X. Sun, R.N. Christensen, I. Skavdahl, V. Utgikar, P. Sabharwall, Pressure drop and heat transfer characteristics of a high-temperature printed circuit heat exchanger, Appl. Therm. Eng. 108 (2016) 1409–1417, https://doi.org/10.1016/j.applthermaleng.2016.07.149.

[23] M. Chen, X. Sun, R.N. Christensen, Thermal-hydraulic performance of printed circuit heat exchangers with zigzag flow channels, Int. J. Heat Mass Transf. 130 (2019) 356–367, https://doi.org/10.1016/j.ijheatmasstransfer.2018.10.031.
[24] A. Meshram, A.K. Jaiswal, S.D. Khivsara, J.D. Ortega, C. Ho, R. Bapat, P. Dutta, Modeling and analysis of a printed circuit heat exchanger for supercritical CO2 power cycle applications, Appl. Therm. Eng. 109 (2016) 861–870, https://doi.org/10.1016/j.applthermaleng.2016.05.033.
[25] T.L. Ngo, Y. Kato, K. Nikitin, N. Tsuzuki, New printed circuit heat exchanger with S-shaped fins for hot water supplier, Exp. Therm. Fluid Sci. 30 (2006) 811–819, https://doi.org/10.1016/j.expthermflusci.2006.03.010.
[26] S.G. Kim, Y. Lee, Y. Ahn, J.I. Lee, CFD aided approach to design printed circuit heat exchangers for supercritical CO2 Brayton cycle application, Ann. Nucl. Energy 92 (2016) 175–185, https://doi.org/10.1016/j.anucene.2016.01.019.
[27] F. Chen, L. Zhang, X. Huai, J. Li, H. Zhang, Z. Liu, Comprehensive performance comparison of airfoil fin PCHEs with NACA 00XX series airfoil, Nucl. Eng. Des. 315 (2017) 42–50, https://doi.org/10.1016/j.nucengdes.2017.02.014.
[28] W.-Q. Wang, Y. Qiu, Y.-L. He, H.-Y. Shi, Experimental study on the heat transfer performance of a molten-salt printed circuit heat exchanger with airfoil fins for concentrating solar power, Int. J. Heat Mass Transf. 135 (2019) 837–846, https://doi.org/10.1016/j.ijheatmasstransfer.2019.02.012.
[29] R.C. Alvarez, A.P.C. Sarmiento, J.V.C. Batista, M.B.H. Mantelli, Entropy generation analysis applied to diffusion-bonded compact heat exchangers, in: AIAA Aviat. 2019 Forum, American Institute of Aeronautics and Astronautics, Dallas, Texas, 2019.
[30] W.M. Kays, A.L. London, Compact Heat Exchangers, third ed., Krieger Publishing Company, USA, n.d.
[31] R.K. Shah, A.L. London, T. Irvine, J.P. Hartnett, Laminar flow forced convection in ducts, in: Adv. Heat Transf., 1978, p. 482.
[32] V. Gnielinski, Heat transfer in pipe flow, in: VDI Heat Atlas, second ed., VDI-Gesellschaft Verfahrenstechnik und Chemieingenieurwesen, Germany, 2010, pp. 693–699.
[33] B.S. Petukhov, Heat transfer and friction in turbulent pipe flow with variable physical properties, in: Adv. Heat Transf, Elsevier, 1970, pp. 503–564, https://doi.org/10.1016/S0065-2717(08)70153-9.
[34] W. Hufschmidt, E. Burck, Der einfluss temperaturabhängiger stoffwerte auf den wärmeübergang bei turbulenter strömung von flüssigkeiten in rohren bei hohen wärmestromdichten und prandtlzahlen, Int. J. Heat Mass Transf. 11 (1968) 1041–1048, https://doi.org/10.1016/0017-9310(68)90009-4.
[35] G.K. Filonenko, Hydraulic resistance in pipes, Teploenergetika 1 (1954) 40–44.
[36] H. Hausen, Wärmeübergang und Druckabfall, vorwiegend in Rohren und Kanälen, in: Wärmeübertragung Im Gegenstrom Gleichstrom Kreuzstrom, Springer Berlin Heidelberg, Berlin, Heidelberg, 1976, pp. 7–123, https://doi.org/10.1007/978-3-642-88686-7_2.
[37] D. Taler, A new heat transfer correlation for transition and turbulent fluid flow in tubes, Int. J. Therm. Sci. 108 (2016) 108–122, https://doi.org/10.1016/j.ijthermalsci.2016.04.022.
[38] A.P.C. Sarmiento, V.H.T. Soares, F.H. Milanese, M.B.H. Mantelli, Heat transfer correlation for circular and non-circular ducts in the transition regime, Int. J. Heat Mass Transf. 149 (2020), https://doi.org/10.1016/j.ijheatmasstransfer.2019.119165.
[39] Y.S. Muzychka, M.M. Yovanovich, Laminar forced convection heat transfer in the combined entry region of non-circular ducts, J. Heat Transf. 126 (2004) 54, https://doi.org/10.1115/1.1643752.
[40] I.H. Bell, J. Wronski, S. Quoilin, V. Lemort, Pure and pseudo-pure fluid thermophysical property evaluation and the open-source thermophysical property library CoolProp, Ind. Eng. Chem. Res. 53 (2014) 2498–2508, https://doi.org/10.1021/ie4033999.
[41] J.P. Holman, Experimental Methods for Engineers, eighth ed., McGraw-Hill/Connect Learn Succeed, Boston, 2012.
[42] ASHRAE, Standard 51, Laboratory Methods of Testing Fans for Aerodynamic Performance Rating, 1999.
[43] J.H. Park, J.G. Kwon, T.H. Kim, M.H. Kim, J.-E. Cha, H. Jo, Experimental study of a straight channel printed circuit heat exchanger on supercritical CO2 near the critical point with water cooling, Int. J. Heat Mass Transf. 150 (2020) 119364, https://doi.org/10.1016/j.ijheatmasstransfer.2020.119364.
[44] I.H. Kim, H.C. No, Thermal–hydraulic physical models for a Printed Circuit Heat Exchanger covering He, He–CO2 mixture, and water fluids using experimental data and CFD, Exp. Therm. Fluid Sci. 48 (2013) 213–221, https://doi.org/10.1016/j.expthermflusci.2013.03.003.
[45] W.M. Kays, R.K. Jain, S. Sabherwal, The effectiveness of a counter-flow heat exchanger with cross-flow headers, Int. J. Heat Mass Transf. 11 (1968) 772–774, https://doi.org/10.1016/0017-9310(68)90078-1.
[46] S. Son, Y. Lee, J.I. Lee, Development of an advanced printed circuit heat exchanger analysis code for realistic flow path configurations near header regions, Int. J. Heat Mass Transf. 89 (2015) 242–250, https://doi.org/10.1016/j.ijheatmasstransfer.2015.05.012.
[47] S. Baek, C. Lee, S. Jeong, Effect of flow maldistribution and axial conduction on compact microchannel heat exchanger, Cryogenics 60 (2014) 49–61, https://doi.org/10.1016/j.cryogenics.2014.01.003.
[48] C.R. Maliska, Transferência de calor e mecânica dos fluidos computacional, Livros Técnicos e Científicos, Rio de Janeiro, 2004.
[49] D.C. Wilcox, Turbulent Modeling of CFD, DCW Industries, San Diego, USA, 2006.